Title: **Association of microglia loss with hippocampal network impairments as a turning point in the amyloid pathology progression.**

Authors: Giusy Pizzirusso[1,2], Efthalia Preka[2#], Julen Goikolea[1#], Celia Aguilar-Ruiz[1], Patricia Rodriguez Rodriguez[1], Guillermo Vazquez Cabrera[3], Simona Laterza[1], Maria Latorre Leal[1], Francesca Eroli[1], Klas Blomgren[2], Silvia Maioli[1], Per Nilsson[1], Adamantia Fragkopoulou[2], André Fisahn[2*], Luis Enrique Arroyo-García[1,2*].

Affiliations: [1]Department of Neurobiology, Care Sciences and Society, Karolinska Institutet, Sweden. [2]Department of Women's and Children's Health, Karolinska Institutet, Sweden. [3]Institute of Environmental Medicine, Toxicology Unit, Karolinska Institutet, Stockholm, Sweden.

Notes: [#]These authors contributed equally

*Co-corresponding authors

Number of Figures: 5 (+8 Supplementary Figures)

Total Word Count: 6343

Abstract: 257

23 **Correspondence to:** Dr. Luis Enrique Arroyo-García[1,2], ORCID: 0000-0002-9206-
24 0179; Dr. André Fisahn[2], ORCID: 0000-0003-1480-175X

25 [1]Division of Neurogeriatrics; Dept. of Neurobiology, Care
26 Sciences and Society; [2]Department of Women's and
27 Children's Health; Karolinska Institutet; Akademiska stråket
28 1; 17164 Solna, Sweden.

29 Email: luis.enrique.arroyogarcia@ki.se; andre.fisahn@ki.se

Abstract

Alzheimer's disease is a progressive neurological disorder causing memory loss and cognitive decline. The underlying causes of cognitive deterioration and neurodegeneration remain unclear, leading to a lack of effective strategies to prevent dementia. Recent evidence highlights the role of neuroinflammation, particularly involving microglia, in Alzheimer's disease onset and progression. Characterizing the initial phase of Alzheimer's disease can lead to the discovery of new biomarkers and therapeutic targets, facilitating timely interventions for effective treatments. We used the *App*$^{NL\text{-}G\text{-}F}$ knock-in mouse model, which resembles the amyloid pathology and neuroinflammatory characteristics of Alzheimer's disease, to investigate the transition from a pre-plaque to an early plaque stage with a combined functional and molecular approach. Our experiments show a progressive decrease in the power of cognition-relevant hippocampal gamma oscillations during the early stage of amyloid pathology, together with a modification of fast-spiking interneuron intrinsic properties and postsynaptic input. Consistently, transcriptomic analyses revealed that these effects are accompanied by changes in synaptic function-associated pathways. Concurrently, homeostasis- and inflammatory-related microglia signature genes were downregulated. Moreover, we found a decrease in Iba1-positive microglia in the hippocampus that correlates with plaque aggregation and neuronal dysfunction. Collectively, these findings support the hypothesis that microglia play a protective role during the early stages of amyloid pathology by preventing plaque aggregation, supporting neuronal homeostasis, and overall preserving the oscillatory network's functionality. These results suggest that the early loss of microglia could be a pivotal event in the progression of Alzheimer's disease, potentially triggering plaque

deposition, impairment of fast-spiking interneurons, and the breakdown of the oscillatory circuitry in the hippocampus.

Keywords: Alzheimer's disease, hippocampal oscillatory network, microglia, fast-spiking interneurons, amyloid pathology.

1 - Introduction

Alzheimer's disease (AD) is a chronic multifactorial disorder characterized by progressive memory loss and cognitive impairment, preceded by a decades-long asymptomatic stage [1]. The events that drive the onset of the pathology leading to cognitive decline and neurodegeneration in the advanced stages remain unclear. This poor understanding of AD aetiopathogenesis is reflected in the absence of early treatment strategies to prevent the onset of dementia rather than slowing down its progression [2,3]. Amyloid beta (Aβ) accumulation is traditionally considered a major AD driver [4,5], however, growing evidence suggests that Aβ amyloidosis alone is not enough to explain the entire AD pathogenesis [6]. Among others, neuroinflammation has been proposed as an important contributor to AD onset and progression [7,8]. Indeed, epidemiological studies have reported a positive association between cognitive decline and previous inflammatory events [9,10]

For this reason, microglia, as the resident immune cell type in the brain, are receiving increasing attention in AD studies. However, whether microglia play a protective or detrimental role during AD progression remains controversial [7,11]. The beneficial role of microglia in containing plaque deposition and delaying cognitive impairment has been reported by several studies [12–16]. Nonetheless, chronic activation of microglia is a well-known cause of neuroinflammation and neurodegeneration [17–19].

Besides their immune-related functions, microglia are involved in homeostatic processes in the brain, including neuronal and network activity regulation [20–23]. One of the consequences of AD is the dysfunction of multiple brain networks, resulting in the inability of the circuits to synchronize in specific oscillation rhythms [24,25]. In particular, brain oscillations in the gamma-frequency band (30-80 Hz) play a pivotal

role in higher brain activities like information processing and memory formation [26–28]. We previously reported that disruption of cognition-relevant gamma oscillations and fast-spiking interneurons (FSI) rhythmicity occurs at an early stage of amyloid pathology in the hippocampus of the *App*$^{NL\text{-}G\text{-}F}$ mouse model [29]. This functional impairment takes place before widespread plaque deposition in the hippocampus. Importantly, restoration of FSI rhythmicity and hippocampal oscillatory activity leads to improved cognitive performance [30,31], underlining the importance of hippocampal network dysfunction in AD pathology progression.

Here, we used a combination of functional and molecular approaches to investigate the mechanisms behind the failure of the hippocampal network and the role of microglia at the earliest stages of amyloid pathology. To our knowledge, this is the first time that such an early pre-plaque stage of amyloidosis progression has been investigated by RNA sequencing in this model. Elucidating the events characterizing the initial phase of the amyloid pathology can generate new perspectives on AD's etiopathogenesis, hence providing new biomarkers and targets for the development of a therapeutic approach to AD based on timely intervention.

2 - Materials and methods

2.1 - Animals

Experiments were performed according to the European and Swedish animal welfare regulations (ethical permit: N45/13 and 12570-2021 approved by Stockholm Animal Ethical Board). Male homozygous *App*$^{NL\text{-}G\text{-}F}$ [32] and wild-type (WT) littermates were bred using the C57/BL6J strain as a background. The mice were sacrificed for brain collection by decapitation under deep anesthetization with isoflurane. Brains were

107 collected between post-natal day (P) 30 and 65 and divided into four representative
108 age points: P30 (P30-35), P40 (P36-45), P50 (P46-55) and P60 (P56-65).

109 ***2.2 - Ex-vivo electrophysiological recordings***

110 Following brain dissection, 350µm thick horizontal hippocampal sections were
111 obtained and kept alive for electrophysiology recordings as previously reported [29].
112 All electrophysiological experiments were performed at a constant temperature of 34
113 °C in a submerged-type recording chamber where slices received a continuous supply
114 of 3 ml/min oxygenated artificial cerebrospinal fluid (ACSF) containing in mM: 124
115 NaCl, 30 NaHCO3, 10 glucose, 1.25 NaH2PO4, 3.5 KCl, 1.5MgCl2, 1.5 CaCl2.
116 Recordings were performed using a Multiclamp 700B amplifier and acquired using
117 pCLAMP 10,4 software (Molecular Devices). Signals were low pass filtered at 1 kHz,
118 acquired at 5 kHz, digitized, and stored using Digidata 1322A and pCLAMP 10,4
119 software (Molecular Devices, CA, USA).

120 ***2.3 - Ex vivo Gamma oscillations***

121 For Local field potential (LFP) measurements, brains from all age points were used:
122 P30 (WT n=6, $App^{NL\text{-}G\text{-}F}$ n=6), P40 (WT n=7, $App^{NL\text{-}G\text{-}F}$ n=6), P50 (WT n=6, $App^{NL\text{-}G\text{-}F}$
123 n=9), P60 (WT n=7, $App^{NL\text{-}G\text{-}F}$ n=11). Ex vivo gamma oscillations were induced by
124 adding kainic acid (KA; Tocris Bioscience, Bristol, UK) at a concentration of 100 nM to
125 the extracellular bath and were recorded using borosilicate glass microelectrodes (1,5-
126 2,5 MΩ) filled with ACSF placed in the stratum oriens of the CA3 area of the
127 hippocampus. The oscillations were allowed to stabilize for at least 20 minutes before
128 recordings were performed. Signals were conditioned using a HumBug 50 Hz noise
129 eliminator (Quest Scientific). For oscillation power spectra Fast Fourier
130 Transformations were obtained from 60 s of LFP recording (segment length 8192

131 points) using Axograph software (Kagi, Berkeley, CA, USA). Frequency variance data
132 was obtained from the power spectra described above using Axograph X. Gamma
133 power was calculated by integrating the power spectral density from 20 to 80 Hz using
134 Clampfit 11.2.

135 ***2.4 - Intrinsic properties of fast-spiking interneurons***

136 Intrinsic properties and spontaneous excitatory post-synaptic currents (sEPSC) were
137 recorded in whole-cell patch clamp mode from fast-spiking interneurons (FSI) in the
138 CA3 stratum radiatum of hippocampal slices from P30 (WT n=17, $App^{NL\text{-}G\text{-}F}$ n=10) and
139 P60 (WT n=11, $App^{NL\text{-}G\text{-}F}$ n=17) brains. Patch clamp recordings were performed with
140 borosilicate glass micropipettes (4–6 MΩ) filled with a potassium-based internal
141 recording solution (in mM: 122.5 K+-gluconate, 8 KCl, 2 Mg2+ ATP, 0,3 Na+ GTP, 10
142 HEPES, 0,2 EGTA, 2 MgCl; pH 7.2–7.3; osmolarity 270–280 mosmol/l) containing 2%
143 of neurobiotin (Vector Laboratories) as a neurotracer. FSI were visualized under an
144 upright microscope using IR-DIC microscopy (Axioskop, Carl Zeis AG, Göttingen,
145 Germany) and identified based on their location, morphology, and response to custom-
146 made current delivery protocols as described previously [29,33]. EPSCs were
147 recorded in voltage-clamp configuration with the voltage holding at -70 mV. Firing and
148 membrane potential properties were recorded in gap-free current-clamp mode. Each
149 cell classified as FSI underwent consequent hyper- and de-polarizing current steps
150 (Input resistance protocol [34]: 25 steps of 10pA from -100pA to +140pA, 700ms each;
151 Fig 2.A) starting from the membrane resting potential and from a -70mV membrane
152 potential. After recording, the slice was stored in PFA overnight and then in a 30%
153 sucrose solution until further experiments. All recordings obtained from FSI were
154 analyzed using a costume-made Python script. sEPSC were analyzed using the Pyabf

155 and Scipy packages. Firing and membrane intrinsic properties were obtained from the
156 abovementioned input resistance protocol using the Pyabf, Ipfx, and Efel packages.

157 • Rehobase (pA), firing threshold (mV), and firing latency (ms) were extracted
158 from the first sweep of the input resistance protocol with at least one action
159 potential.
160 • Mean action potential amplitude (mV), half-width (ms), peak upstroke (V/s),
161 peak downstroke (V/s), rise rate, fall rate, rise time (ms), and fall time (ms) were
162 obtained from the first sweep of the input resistance protocol with four to six
163 action potentials.
164 • Firing rate (Hz) was calculated as the number of action potentials fired during
165 the input resistance protocol, divided by the duration of the protocol.
166 • Ohmic input resistance (GΩ) was calculated by averaging the ohmic input
167 resistance values from subthreshold hyper- and depolarizing current steps in
168 the input resistance protocol (from -30 to +30 mV) in the absence of action
169 potentials.
170 • Membrane potential at the corresponding current step was extracted from each
171 trace of input resistance protocol. Resting membrane potential (Em0)
172 corresponds to the membrane potential when no current is injected.
173 • Sag (mV) was calculated from the most hyperpolarized sweep (-100 pA) of the
174 input resistance protocol recorded with the voltage holding at -70mV.

175 ***2.5 - RT-qPCR***

176 WT (P30 n=4) and *App*$^{NL\text{-}G\text{-}F}$ (P30 n=4, P60 n=4) hippocampal slices were placed in a
177 submerged recording chamber where a solution of ACSF and KA (100 nM) was
178 constantly supplied for 2 hours. After 2 hours, gamma oscillations were recorded to

179 confirm the network activation. For the control group, hippocampal slices from each
180 group were incubated for 2 hours in ACSF without KA.

181 RNA was purified using the PureLink RNA mini kit with in-column DNAse-I digest
182 (#79254, Qiagen) following the manufacturer's instructions (#12183018A,
183 ThermoFisher). RNA was then quantified in a nanodrop and reverse-transcribed using
184 the SuperScript III First-Strand Synthesis System (#18080051, ThermoFisher),
185 followed by RNAse H digestion. cDNA was then used to run qPCRs using TaqMan
186 Universal PCR master mix.

187 FAM-labeled TaqMan assays (ThermoFisher) used were: Mm00463644_m1
188 (*Npas4*), and Mm00487425_m1 (*Fos*). *Gapdh* was used as endogenous control
189 (4352932E). All qPCRs were performed in a 7500 Fast Real-Time PCR system.

190 ***2.6 - RNA extraction and bulk RNA sequencing***

191 Sixteen hippocampi (WT P30 n=4, WT P60 n=4, $App^{NL\text{-}G\text{-}F}$ P30 n=4, $App^{NL\text{-}G\text{-}F}$ P60 n=4)
192 were dissected and used for bulk RNA-seq. Total RNA was isolated using the RNeasy
193 Plus mini kit (QIAGEN #74134) according to the manufacturer's instructions and
194 processed for sequencing at the Bioinformatics and Expression Analysis core facility
195 at Karolinska Institutet. Following the quality control by Agilent Bioanalyzer 2100,
196 samples were processed for library preparation and sequenced using the Illumina
197 Nextseq 2000 P3 (100 cycles) system. All the following analyses were performed in
198 R (version 4.3.0). The DESeq2 (version 1.40,2) package was used to identify
199 differentially expressed genes across different groups. Log fold changes obtained with
200 a Wald test were shrunk using the apelgm method. Statistical significance was
201 considered when adjusted p-value <0,05, as calculated with the Benjamini & Hochberg
202 multiple adjustment method. For the functional classification of DEGs, we used the

203 clusterprofiler [35,36] tool (version 4.8.2). Specifically, Gene Ontology (GO)
204 enrichment analysis was performed to identify the activated and suppressed GO terms
205 (biological processes, molecular function, and cellular component). GO terms that
206 displayed a p-value <0,05, as derived by the hypergeometric test were sorted out as
207 statistically significant. Principal component analysis (PCA) on the sequencing data
208 was performed using the VSN package following instructions from the Bioconductor
209 repository. Centroid coordinates for the PCA plot were calculated as the average of
210 the x and y coordinates of individual samples belonging to the same group.

211 ***2.7 - Western blot***

212 Mouse hippocampal tissue was disrupted and homogenized in 1xRIPA buffer (#89901,
213 Thermo Fisher Scientific) containing phosphatase and protease inhibitors (#P8340
214 and #P0044, Sigma-Aldrich). Homogenates were then centrifuged at 15000×g for
215 15 min 4 °C, and supernatants were mixed with 4X Protein Sample Loading Buffer
216 (#928-40004, LI-COR) containing 2% β-mercaptoethanol (#444203, Sigma-Aldrich).
217 Processed samples were then run in 12.5% homemade polyacrylamide gels (Bio-Rad)
218 and transferred to a 0.45 NC nitrocellulose membranes (Amersham Protran 0.45 NC
219 nitrocellulose membrane, # 10600002, VWR) for 2 h room temperature at 50 V.
220 Membranes were then blocked for 30 minutes in 5% skim milk in 0.1% TBS-Tween-
221 20 (TBS-T) prior to overnight incubation with diluted primary antibody at 4 °C. Primary
222 antibodies: 1:1000 anti-GABA A Receptor alpha 1 polyclonal rabbit antibody
223 (#ab33299, Abcam), 1:1000 anti-Glutamate Receptor 1 (AMPA subtype) polyclonal
224 rabbit antibody (#ab31232, Abcam), 1:10000 anti-GAPDH monoclonal rabbit antibody
225 (#ab8245, Abcam), 1:1000 anti-Iba1 polyclonal rabbit antibody (#ab153696, Abcam),
226 1:1000 anti-HER4/ErbB4 (111B2) Rabbit monoclonal antibody (#4795, Cell Signaling
227 Technology), 1:1000 anti-KCNS3 polyclonal rabbit antibody (#PA5-96856, Invitrogen),

228 1:1000 anti-Nav1.1 Na+ Channel monoclonal mouse antibody (#75-023,
229 Antibodiesinc), 1:1000 anti- KV3.1 (KCNC1) polyclonal rabbit antibody (#PA5-101763,
230 Invitrogen), 1:1000 anti-Synaptotagmin-2 polyclonal rabbit antibody (#60889, Cell
231 Signaling Technology), 1:1000 anti- GABA-A Receptor beta 3 polyclonal rabbit
232 antibody (#NB300-199, Novus Biologocals, Biotechne), 1:500 anti-Glutamate receptor
233 AMPA R4 (#G5790, Sigma-Aldrich). Fluorescent secondary antibodies (1:10000, LI-
234 COR Biosciences) were used for 2 h at room temperature, and bands were visualized
235 using ODYSSEY Infrared Imaging System (LI-COR Biosciences). Band intensity
236 signal was quantified by ImageJ software. Each band signal value was normalized
237 against loading control (GAPDH signal value).

238 ***2.8 - Immunostaining and imaging***

239 Thirty-seven (WT P30 n=11, WT P60 n=9, $App^{NL\text{-}G\text{-}F}$ P30 n=6, $App^{NL\text{-}G\text{-}F}$ P60 n=11)
240 hippocampal slices containing neurobiotin-marked neurons were used for
241 immunostaining. Non-specific binding was blocked by incubating the sections in a
242 solution of 10% normal donkey serum (Jackson ImmunoResearch Laboratories, West
243 Grove, PA), 1.5% Triton X-100 (made Tris buffer saline, TBS) for 2 h at room
244 temperature. Sections were then incubated with primary antibodies rabbit anti-Iba1
245 (1:1000; WAKO) and mouse anti-human amyloid beta 82E1 (1:1000; IBL) at 4°C for
246 48 h and then for 2 h at room temperature with the fluorescent secondary antibodies
247 Alexa-555 donkey anti-rabbit (1:1000; Abcam), Alexa-633 donkey anti-mouse (1:250;
248 Biotium) and Streptavidin 488 (1:1000; Vector laboratories). Hoechst 33342
249 (Molecular Probes/Life Technologies) was used as a nuclear counterstain. Sections
250 were mounted onto glass slides and coverslipped using ProLong diamond anti-fade
251 reagent (Molecular probes/Life technologies). The sections were imaged using a

252 confocal laser scanning microscope (Zeiss LSM900-Airyscan confocal) at the
253 Biomedicum Imaging Core facility at Karolinska Institutet.

254 2.8.1 - Microglia and amyloid plaque density

255 Images of the entire hippocampus were acquired, using a 20x objective, by a
256 combination of tiles and a Z-stack of a thickness of 10µm. These images were
257 processed using the Zen system and their maximum intensity projection was obtained,
258 which allowed for the quantification of the microglia using the Zeiss Zen 3.7 software.
259 Furthermore, the area of the hippocampus was obtained using the lasso tool in the
260 Zeiss software which was also used to acquire the area of the amyloid beta plaques.
261 Microglia and amyloid plaque density as well as plaque area were calculated as a
262 function of the hippocampal area.

263 2.8.2 - Microglia and FSI interaction.

264 In twenty-five of these sections (WT P30 n=6, WT P60 n=6, *App*$^{NL\text{-}G\text{-}F}$ P30 n=6, *App*$^{NL\text{-}G\text{-}F}$ P60 n=6, containing one neurobiotin pre-filled neuron each) images of the
266 neurobiotin-marked neurons were taken at a magnification of 0,7, using a 63x oil
267 objective along with a Z-stack technique of a thickness of 10µm. Subsequently, these
268 images underwent processing utilizing the Zen system: their maximum intensity
269 projections, as well as a subset of images measuring 1355 x 1355 pixels, were
270 generated. Cell surface creation was carried out using the IMARIS 10.0.1 software, by
271 default parameters (surface detail 0.141 µm) in green (AF488) and red (AF555)
272 channels. Surfaces were masked setting a constant in the voxel intensity. Outside
273 surfaces intensity was set to value = 0 and inside surfaces to value =1, generating two
274 new binary channels.

275 Using the IMARIS image processing tool “Channel Arithmetic” by Matlab XTension,
276 the two newly generated binary channels were combined following the formula (chX *
277 chY) resulting in a new channel (pink) that shows only the voxel overlaps from the two
278 binary channels. Voxels with value 1 after the channel arithmetic correspond to the
279 places where voxels of both channels had an overlap in positive signal, indicating the
280 contact surface between cells. Image J software was used to obtain the area of the
281 contacts between microglia and neurons and categorize the contact points into
282 somatic and dendritic.

283 ***2.9 - Statistical analysis***

284 All statistical analyses, excluding the analysis of the bulk RNA sequencing data, were
285 performed using GraphPad Prism 9.4.0. We performed two-sided statistical analyses
286 comparing the *App*$^{NL\text{-}G\text{-}F}$ group and the WT at each age. We used a normality and
287 lognormality test (Shapiro–Wilk test) and we excluded outliers after ROUT (Q = 1%)
288 analysis. We performed one and two-way ANOVA followed by a Holm–Sidak’s multiple
289 comparisons test, unpaired t-test, and Pearson correlation test according to the
290 statistical purpose and number of groups in the analyses. In the graphs data are
291 reported as means ± SEM and significance levels are *p < 0,05, **p < 0,01, ***p <
292 0,001, **** p < 0,0001. The three-dimensional PCA of neuronal properties was
293 performed in Phyton using the Sklearn package.

294

295 **3 - Results**

296 **3.1 - Progressive impairment of hippocampal gamma oscillations in *App*$^{NL\text{-}G\text{-}F}$**
297 **mice.**

298 Previous evidence from our lab shows an early impairment in the hippocampal
299 oscillatory activity during amyloid pathology progression in the *App*$^{NL\text{-}G\text{-}F}$ knock-in
300 mouse model [29]. We reported that gamma oscillations were strongly decreased in
301 the *App*$^{NL\text{-}G\text{-}F}$ mice at P75 when compared to age-matched WT mice, while no
302 differences were observed at P30 [29]. In the present study, we first aimed to narrow
303 down the time-point when this shift in hippocampal gamma oscillations occurs. For this
304 purpose, we investigated ex vivo gamma oscillations in hippocampal slices of *App*$^{NL\text{-}}$
305 $^{G\text{-}F}$ and WT mice at P30, P40, P50, and P60 (Fig 1.A).

306 *App*$^{NL\text{-}G\text{-}F}$ mice exhibited a progressive decrease in gamma power that is significant at
307 P50 compared to P30 mice (*App*$^{NL\text{-}G\text{-}F}$ P30 vs P50 p=0,027; Fig 1.B, C). Additionally,
308 we confirmed that gamma oscillations were comparable in power comparing the
309 *App*$^{NL\text{-}G\text{-}F}$ and WT groups at P30 (WT vs *App*$^{NL\text{-}G\text{-}F}$ P30 p=0,190; Fig 1.C), while they
310 were significantly decreased at P50 in the *App*$^{NL\text{-}G\text{-}F}$ group as compared to age-
311 matched WT mice (WT vs *App*$^{NL\text{-}G\text{-}F}$ P60 p=0,041; Fig 1.C). This gamma oscillation
312 impairment in *App*$^{NL\text{-}G\text{-}F}$ mice continued to decrease at P60 (WT vs *App*$^{NL\text{-}G\text{-}F}$ P60
313 p=0,082, *App*$^{NL\text{-}G\text{-}F}$ P30 vs P60 p=0,014; Fig 1.C). No change was detected in
314 frequency variance (Supp fig 1.A) and peak frequency (Supp fig 1.B).

315 These results provide a specific time window to investigate the functional and
316 molecular changes in this early stage of amyloid pathology progression and potentially
317 identify new targets to prevent and/or recover them. Therefore, we selected a time
318 point in the *App*$^{NL\text{-}G\text{-}F}$ mice where the oscillatory activity is comparable to the WT mice
319 (P30) and a time point with oscillatory impairment (P60) for further analysis.

320 After selecting the time points of interest, we next asked if the induction of hippocampal
321 gamma oscillations by KA could promote the expression of immediate early genes

322 (IEG). IEG are rapidly induced in response to neuronal depolarization and play an
323 essential role in neuronal synaptic plasticity and learning-associated processes [37–
324 40]. We therefore quantified *Fos* and *Npas4* gene expression analysis by RT-qPCR
325 in KA-exposed hippocampal slices before and after gamma oscillation impairment in
326 *App*$^{NL\text{-}G\text{-}F}$ mice and compared them to a WT group (Fig 1.A).

327 Our results show that the network activation with KA caused an induction of *Fos* (Fig
328 1.D, p=0,0005) and *Npas4* (Fig 1.E, p=0,0014) expression in WT mice. This effect was
329 not observed in *App*$^{NL\text{-}G\text{-}F}$ mice at P30 nor at P60 (Fig 1.D, E), in line with previous
330 studies that report suppression of IEG in the presence of Aβ [41].

331

332 **3.2 - Fast-spiking interneuron intrinsic properties and postsynaptic input**
333 **change during amyloid pathology progression.**

334 Fast-spiking interneurons (FSI) are a subtype of GABAergic interneurons that hold a
335 pivotal role in initiating and sustaining gamma oscillations [42–44]. We have previously
336 reported that FSI spike-gamma coupling is affected during amyloid pathology
337 progression at P75 [29]. Here we aimed to assess the functionality of FSI in the *App*$^{NL\text{-}}$
338 $^{G\text{-}F}$ mice. For this reason, we used the whole-cell patch-clamp technique to assess the
339 intrinsic properties and post-synaptic currents of FSI in a resting state (without KA) in
340 WT and *App*$^{NL\text{-}G\text{-}F}$ mice at P30 and P60 (Fig 2.A; Table 1).

341 To evaluate differences and similarities within FSI across all groups, we performed a
342 three-dimensional principal component analysis (PCA) on the intrinsic properties of
343 FSI (Table 1). This analysis revealed that FSI in the *App*$^{NL\text{-}G\text{-}F}$ group at P60 had
344 distinctive intrinsic properties since they clustered in a separate area of the plot
345 compared to the *App*$^{NL\text{-}G\text{-}F}$ group at P30 and the WT groups at P30 and P60 (Fig 2.C;

346 supp. video 1). This result indicates that FSI in the *App*$^{NL\text{-}G\text{-}F}$ mice at P30 were
347 functionally comparable to those from the WT groups, while at P60 they diverged from
348 the WT groups and the *App*$^{NL\text{-}G\text{-}F}$ P30 group, implying an alteration of FSI intrinsic
349 properties during amyloidosis progression (*App*$^{NL\text{-}G\text{-}F}$ P30 vs P60; Fig 2.B). Indeed, FSI
350 in the *App*$^{NL\text{-}G\text{-}F}$ group at P60 were depolarized (p=0,044; Fig 2.D), and they exhibited
351 a higher firing threshold (p=0,011; Fig 2.E) and faster repolarization phase of the action
352 potential (p=0,049; Fig 2.F) in comparison with FSI in the *App*$^{NL\text{-}G\text{-}F}$ group at P30.
353 Additionally, FSI from P60 *App*$^{NL\text{-}G\text{-}F}$ mice received a decreased postsynaptic input, as
354 shown by charge transfer (p=0,027, Fig 2.G) and spontaneous excitatory postsynaptic
355 current (sEPSC) frequency (p=0,027, Fig 2.H). These findings suggest a change in
356 the FSI membrane properties during the amyloid pathology progression. Importantly,
357 the properties that differed between *App*$^{NL\text{-}G\text{-}F}$ P60 and P30 were preserved in the
358 *App*$^{NL\text{-}G\text{-}F}$ P30 group as compared to age-matched WT mice (Supp fig 2), confirming
359 that the functionality of FSI was not affected at this time point.

360 Collectively, such changes in FSI functionality might contribute to the impairment of
361 the hippocampal network (Fig 1.B, C) and the FSI spike-gamma uncoupling [29] that
362 we observed in the early stage of the amyloid pathology progression.

363

364 **3.3 - Bulk RNA sequencing reveals synaptic-related transcriptional changes**
365 **during the early stage of amyloid pathology progression.**

366 Next, we performed bulk RNA sequencing to investigate the molecular events before
367 and after the impairment in the hippocampal oscillatory activity and neuronal
368 properties in the *App*$^{NL\text{-}G\text{-}F}$ mouse model (Fig 3.A).

369 First, we analyzed the dataset from WT mice at P30 vs P60, showing 998 differentially
370 expressed genes (DEG) plausibly due to brain maturation (Supp fig 3.A). Then we
371 compared age-matched WT vs *App*$^{NL\text{-}G\text{-}F}$ groups at P30 and P60 age to evaluate the
372 amyloidogenic effect in the *App*$^{NL\text{-}G\text{-}F}$ knock-in model in comparison to WT mice. We
373 found 510 DEG at P30 WT vs *App*$^{NL\text{-}G\text{-}F}$ (Supp fig 4.A) and 930 DEG at P60 WT vs
374 *App*$^{NL\text{-}G\text{-}F}$ (Supp fig 4.B). Finally, to assess the effects of amyloid pathology progression
375 we compared the *App*$^{NL\text{-}G\text{-}F}$ model at P30 vs P60 and we found 4246 DEG (Supp fig
376 3.B).

377 To differentiate the transcriptional changes triggered by amyloid pathology (App$^{NL\text{-}G\text{-}F}$
378 P30 vs P60) from the ones due to normal brain maturation (WT P30 vs P60), we
379 compared the DEGs from these two groups (Fig. 3.B). We found that 686 DEGs (120
380 upregulated and 588 downregulated; supp fig 5.A) were shared between the two
381 comparisons, suggesting that it is genes that are indeed associated with brain
382 maturation in both WT and *App*$^{NL\text{-}G\text{-}F}$ mice. Interestingly, 3560 DEG (1673 upregulated
383 and 1887 downregulated, supp fig 5.A) changed exclusively during amyloid pathology
384 progression (*App*$^{NL\text{-}G\text{-}F}$ P30 vs P60).

385 Next, to find the biological pathways involved in the transcriptional changes we
386 performed an enrichment analysis (Supp. Table 2) at P30 (WT P30 vs *App*$^{NL\text{-}G\text{-}F}$ P30,
387 supp fig 5.B), at P60 (WT P60 vs *App*$^{NL\text{-}G\text{-}F}$ P60, supp fig 5.C), during brain maturation
388 (WT P30 vs P60, supp fig 5.D) and amyloid pathology progression (*App*$^{NL\text{-}G\text{-}F}$ P30 vs
389 P60, fig 3.D). Our analysis reveals the activation of synaptic pathways in the *App*$^{NL\text{-}G\text{-}}$
390 ^{F} group compared to the WT at P30 (WT P30 vs *App*$^{NL\text{-}G\text{-}F}$ P30, Supp Fig 5.B). In
391 contrast, at P60, the enrichment analysis shows fewer synaptic pathways when we
392 compare the *App*$^{NL\text{-}G\text{-}F}$ and WT groups (WT P60 vs *App*$^{NL\text{-}G\text{-}F}$ P60, Supp Fig 5.C).
393 Moreover, we found that the synaptic pathways were scarcely affected by maturation

394 (WT P30 vs P60 Supp Fig 5.D). Interestingly, multiple pathways related to synaptic
395 transmission, GABAergic and glutamatergic communication, ion channel activity,
396 synaptic communication, and membrane potential and action potential regulation were
397 activated during amyloid pathology progression (Fig 3.D). Candidate genes belonging
398 to these pathways were selected based on their involvement in gamma oscillations
399 and FSI functionality as potential causes of early functional impairment during amyloid
400 pathology progression. *Kcnc1* [45–47], *Kcns3* [48,49], *Scn1a* [50,51], *Erbb4* [52–55],
401 *GABRA1* [56,57] and *Syt2* [58–61] were upregulated in the $App^{NL\text{-}G\text{-}F}$ group at P60 (Fig
402 3.C; Supp table 1).

403 After, we aimed to investigate whether the transcriptional changes during amyloidosis
404 pathology progression detected by RNA sequencing translated to protein level
405 changes ($App^{NL\text{-}G\text{-}F}$ P30 vs P60). For this purpose, we quantified specific proteins
406 corresponding to the altered genes in our transcriptomic assessment (ErbB4, KCNS3,
407 Nav 1.1, Kv 3.1, Syt 2, GABA A b3, and GluR4) and some additional receptor subunits
408 involved in the FSI and gamma oscillations activity: Glutamate receptor A1, GABA
409 receptor A beta3 [31] and glutamate receptor 4 [62]. Our results showed that GABA
410 receptor 1 alpha (Fig. 3.E, F) and glutamate receptor A1 (Fig. 3.E, G) were significantly
411 downregulated already at P30 in the $App^{NL\text{-}G\text{-}F}$ mice when compared to WT mice, and
412 the downregulation is also detected at P60. No other changes in protein levels were
413 detected at these time points (Supp Fig 6).

414

415 **3.4 - Microglia-related transcriptional changes indicate loss of homeostatic and**
416 **inflammatory microglia during the early stage of amyloid pathology**
417 **progression.**

418 Given the crucial role of microglia in neuronal network regulation [21] and AD [7,63],
419 our next step was to investigate transcriptional changes of microglia-related genes
420 and pathways.

421 Pathway enrichment analysis (Supp. Table 2) showed that microglia- and
422 inflammation-related processes, including microglia differentiation, acute inflammatory
423 response, phagocytosis, synaptic pruning, and complement systems were suppressed
424 in the *App*$^{NL\text{-}G\text{-}F}$ group at P60 compared to P30 (*App*$^{NL\text{-}G\text{-}F}$ P30 vs P60; Supp fig 7.A).
425 Interestingly, similar pathways are activated in *App*$^{NL\text{-}G\text{-}F}$ mice at P30 compared to age-
426 matched WT mice (WT vs *App*$^{NL\text{-}G\text{-}F}$ P30; Supp fig 7.B). Fewer microglia and
427 inflammation-related changes occur with normal brain maturation in the WT group (WT
428 P30 vs P60; Supp fig 7.C) and in the *App*$^{NL\text{-}G\text{-}F}$ group at P60 compared to age-matched
429 WT mice (WT vs *App*$^{NL\text{-}G\text{-}F}$ P60; Supp fig 7.D). These transcriptional changes suggest
430 a general activation of microglia and inflammation-related pathways in the *App*$^{NL\text{-}G\text{-}F}$
431 group at P30, followed by their suppression at P60.

432 Furthermore, we evaluated the transcriptional differences of microglia populations
433 across the four groups using a two-dimensional PCA. We selected 2054 microglia
434 genes, representative of homeostatic and inflammatory microglia [64–66] from the
435 RNA sequencing dataset (Supp. Table 3). The PCA underlines the similarity of the
436 microglia expression profiles in the WT group at P30 and P60. Conversely, microglia
437 gene expression differs between P30 and P60 in the *App*$^{NL\text{-}G\text{-}F}$ mice, with samples from
438 P30 and P60 time points clustering separately at the opposite edges of the PCA plot
439 (Fig. 4.A). A similar sample distribution can be observed when genes representative
440 of single microglia populations are plotted separately (Homeostatic and pruning
441 microglia, 751 genes, Supp fig 8.A; activated microglia, 885 genes, Supp fig 8.B;
442 interferon responding microglia, 418 genes, Supp fig 8.C). This result suggests that

443 the microglia transcriptional profile changes to a higher extent during amyloid
444 pathology progression than it would during normal maturation.

445 To further characterize this event, we analyzed the expression of distinctive genes for
446 different subpopulations of microglia previously reported by single-nucleus RNA
447 sequencing characterization of microglia in the *App*$^{NL\text{-}G\text{-}F}$ mouse model [64]:
448 *Tmem119, P2ry12,* and *Cx3cr1* for homeostatic microglia; *C1qa, C1qb, C1qc, Ctsb,*
449 *Ctsd, Fth1* and *Lyz2* homeostatic microglia engaged in synaptic pruning; *Irf7, Ifitm3,*
450 *Ifit3, Oasl2, Ifitm1* and *Ifit2* for interferon responding microglia; *Clec7a, Cst7* and *Itgax*
451 for activated response microglia. A significant downregulation of genes related to
452 microglia homeostatic and inflammatory states was detected in the *App*$^{NL\text{-}G\text{-}F}$ group at
453 P60 compared to P30 (*App*$^{NL\text{-}G\text{-}F}$ P30 vs P60; Fig 4.B). Additionally, widely accepted
454 pan-microglia markers such as *Aif1, Fcrls,* and *Hexb* [67] followed the same
455 expression pattern, suggesting a suppression of microglia-related genes in *App*$^{NL\text{-}G\text{-}F}$
456 mice at P60 that could indicate a loss of microglia at this time point. To test this
457 hypothesis, we measured the protein levels of Iba1, which is the protein encoded by
458 *Aif1* and a commonly used pan-microglia marker, by western blot (Fig 4.C, D). The
459 level of Iba1 increased in P30 *App*$^{NL\text{-}G\text{-}F}$ mice compared to age-matched WT mice (WT
460 vs *App*$^{NL\text{-}G\text{-}F}$ P30, p=0,009; fig 4.C) and decreased between P30 and P60 in the *App*$^{NL\text{-}}$
461 $^{G\text{-}F}$ group (*App*$^{NL\text{-}G\text{-}F}$ P30 vs P60, p=0,013; fig 4.C).

462

463 **3.5 - Iba1-positive microglia density decreases during the early stage of amyloid**
464 **pathology and correlates with plaque aggregation and FSI dysfunction.**

465 To verify that the microglia-related transcriptional and protein level variations reflected
466 a change in the density of microglia in the hippocampus of *App*$^{NL\text{-}G\text{-}F}$ mice, we

467 performed immunofluorescence staining (Fig 5.A-D) of hippocampal slices containing
468 neurobiotin-marked FSI from our intracellular recordings (Fig 5.I, 2.A).

469 Here we showed that microglia density, expressed as the number of Iba1-positive cells
470 by area, increased at P30 in *App*$^{NL\text{-}G\text{-}F}$ mice compared to age-matched WT mice (WT
471 vs *App*$^{NL\text{-}G\text{-}F}$ P30, p=0.036; fig 5.K). Importantly, we found a decrease in the
472 hippocampus of *App*$^{NL\text{-}G\text{-}F}$ mice at P60 when compared to P30 (*App*$^{NL\text{-}G\text{-}F}$ P30 vs P60,
473 p<0,0001; fig 5.K). These findings validate the dynamic pattern of microglia abundance
474 and gene expression observed by the transcriptomic and protein analysis.

475 Besides microglia, we stained Aβ to evaluate the stage of plaque development during
476 amyloid pathology progression in the hippocampus. As expected, the hippocampi of
477 WT mice were free of amyloid plaques (Fig 5.A,B). In contrast, we found small, non-
478 widespread amyloid plaques in the hippocampi of *App*$^{NL\text{-}G\text{-}F}$ mice at P60, but not at
479 P30 (Fig 5.C-D, J). Interestingly, the area occupied by amyloid plaques inversely
480 correlated with the density of Iba1-positive microglia in the hippocampus of P60 *App*$^{NL\text{-}}$
481 $^{G\text{-}F}$ mice (Fig 5.M), suggesting that the loss of microglia could play a role in plaque
482 aggregation at this stage of the pathology. Additionally, to investigate whether the loss
483 of Iba1-positive microglia in P60 *App*$^{NL\text{-}G\text{-}F}$ mice affected the interaction between
484 microglia and FSI, we used Imaris to obtain a 3D reconstruction of neurobiotin-marked
485 FSI, labeled during patch-clamp recordings, and microglia (Fig 5.E-H). We found that
486 the somatic contact area between microglia and FSI is decreased at P60 when
487 compared to P30 in *App*$^{NL\text{-}G\text{-}F}$ mice (*App*$^{NL\text{-}G\text{-}F}$ P30 vs P60, p=0,069; fig 5.L), while the
488 number of contacts is similar between *App*$^{NL\text{-}G\text{-}F}$ P30 and WT P30 and P60 (Fig 5.L).

489 Since somatic microglia-neuron interaction has been reported to regulate neuronal
490 activity and excitability [22,68], we explored a potential connection between the area

491 of microglia-FSI somatic interphase and FSI excitability in all the groups. To this end,
492 we tested the correlation between microglia-FSI contact area and the FSI intrinsic
493 properties that were affected in P60 *App*$^{NL-G-F}$ mice (Fig 2.D-F), adding the firing rate
494 as an additional parameter to evaluate excitability. Interestingly, the microglia-FSI
495 somatic contact area positively correlated with FSI firing rate and negatively with their
496 firing threshold, indicating that FSI with a smaller microglia-FSI somatic interphase
497 area had a higher firing threshold (p=0,015) and fired at a lower rate (p=0,023, Fig
498 5.N).

499 Taken together, our results show a higher density of Iba1-positive microglia in the
500 hippocampus of *App*$^{NL-G-F}$ mice compared to WT before plaque deposition and
501 functional impairment, which decreases one month later, in correspondence with the
502 beginning of amyloid plaque aggregation and network dysfunction. In addition, this
503 loss of microglia in the *App*$^{NL-G-F}$ group at P60 is associated with changes in the firing
504 activity of FSI, through a lack of microglia-FSI somatic contacts.

505

506 **4 - Discussion**

507 In this study, we show that amyloid pathology in *App*$^{NL-G-F}$ mice progressively and
508 detrimentally affects the hippocampal circuit responsible for gamma oscillations to a
509 point of network failure, before widespread Aβ plaque load. Concurrently, the intrinsic
510 properties of FSI are compromised during this early stage of the pathology.
511 Interestingly, we found that this early functional impairment is associated with a loss
512 of Iba1-positive microglia in the hippocampus and a decrease in their somatic contacts
513 with FSI. We propose that this loss of microglia could be connected to the onset of Aβ
514 plaque aggregation and network dysfunction in the hippocampus.

515 Increasing evidence has shown a crucial role of microglia in AD pathogenesis and
516 progression [7,63]. However, the involvement of this cell type in AD pathology
517 development and its role in Aβ plaque formation and clearance remains controversial
518 [7,11]. One of the main difficulties to overcome when studying microglia is their
519 extreme dynamism, the reason why different studies can lead to apparently
520 contradictory results when trying to shed light on their role in AD pathophysiology.
521 Studies have shown the protective function of microglia activation at pre-symptomatic
522 stages of amyloidosis both in animal models [12,15] and clinical studies [13,17].
523 Indeed, in patients in a preclinical stage of AD, microglia activation correlated with a
524 slower cognitive decline [13] and amyloid deposition [14]. Recently, Yang et al.
525 reported that priming microglia before plaque aggregation promotes Aβ phagocytosis,
526 reduces the size of Aβ plaques, and improves memory performance in 5xFAD mice
527 [15].

528 On the other hand, the contribution of microglia to plaque formation and compaction
529 has been hypothesized [69–71]. In particular, Spangenberg et al. reported that
530 microglia depletion impairs Aβ plaque formation in 5xFAD mice [71]. The mechanism
531 behind this process remains unclear. One hypothesis is that excessive accumulation
532 of Aβ in microglia lysosomes leads to cell death, which might promote plaque
533 aggregation by the release of Aβ agglomerates at the site of microglial death [72].
534 Additionally, strong evidence suggests that microglia reactivity promotes
535 neurodegeneration by sustaining chronic inflammation at advanced AD stages [17,19].
536 In agreement with all these findings, a biphasic model has been proposed to explain
537 microglia changes during AD progression. First, a protective peak of microglia
538 activation arises in an early pre-symptomatic stage of the pathology, before Aβ plaque

539 formation. Then a second detrimental activation phase promoting neuroinflammation
540 takes place [14,63,73].

541 In this study, we found an increased density of Iba1-positive microglia in the
542 hippocampus of *App*$^{NL\text{-}G\text{-}F}$ mice compared to WT (Fig 5.K) at a timepoint (P30) that
543 precedes Aβ plaque aggregation (Fig 5.C, J) and functional impairment (Fig 1.B-C).
544 An increased number of microglia cells is considered a sign of microglia activation
545 during inflammatory response [74,75], in line with studies reporting an inflammatory
546 response of microglia before plaque formation in animal models of amyloid pathology
547 [18,76–78]. This suggests microglia activation in response to Aβ clearing, which keeps
548 the brain free of Aβ plaques and maintains the hippocampal synaptic function.

549 However, as the pathology progresses in the *App*$^{NL\text{-}G\text{-}F}$ mice (P60), we observe a loss
550 of Iba1-positive microglia in comparison to the initial increase (P30; Fig 5.K). This takes
551 place concurrently with the onset of functional impairment (Fig 1.B) and Aβ plaque
552 aggregation (Fig 5.D, J) in the hippocampus. Moreover, homeostatic and inflammatory
553 microglia genes [64] are downregulated at P60 compared to P30 (Fig 4.B), suggesting
554 that the reduction in the number affects in general the diverse microglia populations.
555 Furthermore, in our samples the density of Iba1-positive microglia in the hippocampus
556 negatively correlated with the hippocampal area occupied by Aβ plaques (Fig 5.M),
557 suggesting that microglia loss might facilitate Aβ plaque aggregation at this time point.

558 While late microglia states in the *App*$^{NL\text{-}G\text{-}F}$ mouse model have been observed and
559 characterized [64], this is the first time that an increased density of microglia is
560 detected in a pre-plaque stage in this model. Although the causes and mechanisms
561 behind the switch from protective to detrimental microglia remain to be elucidated [7],

562 our findings of microglia loss between the two activation peaks could represent a
563 turning point in this dynamic process.

564 Furthermore, we show that this decrease in Iba-1 positive microglia affects not only
565 the total microglia number in the hippocampus but, importantly, its somatic contacts
566 with FSI, which are also decreased (Fig 5.L). Microglia dynamically interact with
567 neurons, constantly monitoring and regulating their activity [79]. Somatic junctions
568 between microglia and neurons play a key role in this homeostatic communication
569 [22,80]. Interestingly, in addition to decreased somatic contacts between microglia and
570 FSI, we observed a downregulation of *P2y12r* (Fig 4.B), a purinergic receptor that is
571 fundamental for microglia-neuron crosstalk [22], suggesting a loss of homeostatic
572 surveillance of microglia on FSI. When somatic microglia-neuron interaction is
573 compromised, changes in neuronal activity and excitability have been reported [22,68].
574 Consistently, our data show a change in FSI's membrane and firing properties and a
575 decrease in their postsynaptic input (Fig 2).

576 We found that microglia-FSI somatic contact area correlated positively with FSI firing
577 rate and negatively with FSI firing threshold, which implies that FSI with smaller
578 somatic contacts with microglia had a higher firing threshold and a lower firing rate
579 (Fig 5.N). Our findings support the role of microglia surveillance in regulating FSI
580 homeostasis, suggesting that a change in microglia-FSI somatic contacts can affect
581 FSI excitability.

582 FSI are a subpopulation of inhibitory interneurons that, due to their specific firing
583 properties [81–83], synchronize the hippocampal network in the gamma rhythm (20-
584 80 Hz) [42,44,84]. Gamma oscillations are associated with higher cognitive functions
585 [27], specifically hippocampal gamma oscillations are involved in memory formation

586 and learning processes [26,28]. Alterations in gamma oscillation onset are related to
587 cognitive deficits in multiple neurodegenerative diseases, including AD [85]. High
588 concentrations of Aβ were reported to degrade hippocampal gamma oscillations in an
589 acute amyloidogenic model [86]. Furthermore, we have proven that amyloid pathology
590 leads to FSI desynchronization and gamma oscillation disruption, before widespread
591 Aβ plaque deposition in the hippocampus of *App*$^{NL\text{-}G\text{-}F}$ mice [29]. We have now shown
592 that resting membrane potential, firing threshold, action potential repolarization phase
593 as well as postsynaptic current frequency and amplitude (Fig 2) of FSI change during
594 amyloid pathology progression. These neuronal properties are crucial to regulate the
595 intrinsic excitability of FSI [87], hence their modification can explain the FSI loss of
596 rhythmicity and the consequent network failure that we observed in the hippocampus
597 of *App*$^{NL\text{-}G\text{-}F}$ mice at P75 in our previous study [29]. Interestingly, restoration of FSI
598 firing properties and rhythmicity leads to an improvement of gamma oscillation
599 synchrony and cognitive performance [29,31,62].

600 Our transcriptomic analysis revealed that multiple pathways and genes related to
601 synaptic transmission and neuronal excitability regulation are activated in
602 correspondence with the hippocampal network dysfunction in the *App*$^{NL\text{-}G\text{-}F}$ model (Fig
603 3.C, D). Additionally, the protein expression of GABA receptor 1 alpha (Fig 3. F) and
604 glutamate receptor A1 protein levels were decreased in the App$^{NL\text{-}G\text{-}F}$ group at P30 and
605 60 (Fig 3.G). These receptor subunits belong to the main inhibitory and excitatory
606 receptors expressed in the hippocampus, namely GABA A [56] and AMPA [88]. Given
607 the importance of AMPA transmission for synaptic plasticity, this finding could explain
608 the lack of increased IEG expression in App$^{NL\text{-}G\text{-}F}$ mice upon KA-induced neuronal
609 activation (Fig. 1.C, D) [89].

610 Here we propose that microglia play a protective role at earlier stages of amyloidosis
611 preventing plaque aggregation and supporting FSI physiological functionality, which
612 results in a preserved network synchronization in the gamma rhythm. Conversely,
613 microglia loss in the early stage of amyloid pathology progression might facilitate
614 plaque aggregation, cause functional impairment in FSI, and, consequently, prevent
615 the synchronization of the hippocampal network in the gamma rhythm.

616

617 **5 - Conclusions**

618 In conclusion, here we identified for the first time a loss of microglia during the early
619 stage of amyloid pathology, before the manifestation of widespread Aβ plaque load in
620 the hippocampus. Our findings suggest that microglia loss might represent a turning
621 point in AD pathology progression, contributing to Aβ plaque formation, FSI
622 dysfunction, and circuit failure in the hippocampus.

Declarations

Ethical approval

Experiments were performed in accordance with the ethical permit granted by Norra Stockholm's Djurförsöksetiska Nämnd (dnr N45/13) to AF and 12570-2021 to PN.

Consent for publication

Not applicable

Availability of data and materials

Raw data is available from the corresponding authors upon request.

Competing of interest

The authors declare that they have no competing interests to disclose.

Funding

This work was supported by the StratNeuro program and the Foundation for Geriatric Diseases at Karolinska Institutet, the Stohnes Stiftelse, Stiftelse För Gamla Tjänarinnor (LEAG), the Swedish Research Council, the Swedish Brain Foundation, and the Swedish Alzheimer Foundation (AF), KI/NIH Doctoral Partnership Programme in Neuroscience (AF/KB) and Margaretha af Ugglas Stiftelse (PRR).

Authors contributions

LEAG and AF designed the experiments. GP, LEAG, JG, CAR, SL, PRR, EP, GVC, MLL, FE, SM, PN, AFr, and KB performed experiments and analyses. GP created the Python scripts for analysis. GP and LEAG wrote the paper with inputs from all co-authors.

Acknowledgments

We thank Simon Sundström for the guidance and help with the Python scripts and Johanna Wanngren for the help with mouse breeding. We thank Takaomi Saido and Takashi Saito at RIKEN Center for Brain Science, Japan for providing App knock-in mice.

655 **References**

656 1. Aisen PS, Cummings J, Jack CR, Morris JC, Sperling R, Frölich L, et al. On the path
657 to 2025: Understanding the Alzheimer's disease continuum. Alzheimers Res Ther.
658 BioMed Central Ltd.; 2017.

659 2. Golde TE. Disease-Modifying Therapies for Alzheimer's Disease: More Questions
660 than Answers. Neurotherapeutics. Springer Science and Business Media Deutschland
661 GmbH; 2022. p. 209–27.

662 3. Mehta D, Jackson R, Paul G, Shi J, Sabbagh M. Why do trials for Alzheimer's
663 disease drugs keep failing? A discontinued drug perspective for 2010-2015. Expert
664 Opin Investig Drugs. 2017;26:735–9.

665 4. Braak H, Braak E. Neuropathological stageing of Alzheimer-related changes. Acta
666 Neuropathol. 1991;82:239–59.

667 5. Hardy J, Selkoe DJ. The Amyloid Hypothesis of Alzheimer's Disease: Progress and
668 Problems on the Road to Therapeutics. Science (1979) [Internet]. 2022;297:353–6.
669 Available from: https://www.science.org

670 6. Herrup K. The case for rejecting the amyloid cascade hypothesis. Nat Neurosci.
671 2015;18:794–9.

672 7. Leng F, Edison P. Neuroinflammation and microglial activation in Alzheimer disease:
673 where do we go from here? Nat Rev Neurol. Nature Research; 2021. p. 157–72.

674 8. Passamonti L, Tsvetanov KA, Jones PS, Bevan-Jones WR, Arnold R, Borchert RJ,
675 et al. Neuroinflammation and functional connectivity in Alzheimer's disease: Interactive
676 influences on cognitive performance. Journal of Neuroscience. 2019;39:7218–26.

677 9. Holmes C. Comment Common infections and increased risk of developing
678 dementia : compelling evidence for intervention studies. Lancet Healthy Longev.
679 2021;2:e391–2.

680 10. Bohn B, Lutsey PL, Misialek JR, Walker KA, Brown CH, Hughes TM, et al.
681 Incidence of Dementia Following Hospitalization With Infection Among Adults in the
682 Atherosclerosis Risk in Communities (ARIC) Study Cohort. JAMA Netw Open.
683 2023;6:e2250126.

684 11. Hamelin L, Lagarde J, Dorothée G, Potier MC, Corlier F, Kuhnast B, et al. Distinct
685 dynamic profiles of microglial activation are associated with progression of Alzheimer's
686 disease. Brain. 2018;141:1855–70.

687 12. Feng W, Zhang Y, Wang Z, Xu H, Wu T, Marshall C, et al. Microglia prevent beta-
688 Amyloid plaque formation in the early stage of an Alzheimer's disease mouse model
689 with suppression of glymphatic clearance. Alzheimers Res Ther. 2020;12:1–15.

690 13. Hamelin L, Lagarde J, Dorothée G, Leroy C, Labit M, Comley RA, et al. Early and
691 protective microglial activation in Alzheimer's disease: A prospective study using 18F-
692 DPA-714 PET imaging. Brain. 2016;139:1252–64.

693 14. Fan Z, Brooks DJ, Okello A, Edison P. An early and late peak in microglial activation
694 in Alzheimer's disease trajectory. Brain. 2017;140:792–803.

695 15. Yang Y, García-Cruzado M, Zeng H, Camprubí-Ferrer L, Bahatyrevich-Kharitonik
696 B, Bachiller S, et al. LPS priming before plaque deposition impedes microglial
697 activation and restrains Aβ pathology in the 5xFAD mouse model of Alzheimer's
698 disease. Brain Behav Immun. 2023;113:228–47.

699 16. Femminella GD, Dani M, Wood M, Fan Z, Calsolaro V, Atkinson R, et al. Microglial
700 activation in early Alzheimer trajectory is associated with higher gray matter volume.
701 Neurology. 2019;92:E1331–43.

702 17. Fan Z, Aman Y, Ahmed I, Chetelat G, Landeau B, Ray Chaudhuri K, et al. Influence
703 of microglial activation on neuronal function in Alzheimer's and Parkinson's disease
704 dementia. Alzheimer's and Dementia. 2015;11:608-621.e7.

705 18. Heneka MT, Sastre M, Dumitrescu-Ozimek L, Dewachter I, Walter J, Klockgether
706 T, et al. Focal glial activation coincides with increased BACE1 activation and precedes
707 amyloid plaque deposition in APP[V717I] transgenic mice. J Neuroinflammation.
708 2005;2:1–12.

709 19. Mass E, Jacome-Galarza CE, Blank T, Lazarov T, Durham BH, Ozkaya N, et al. A
710 somatic mutation in erythro-myeloid progenitors causes neurodegenerative disease.
711 Nature. 2017;549:389–93.

712 20. Karson MA, Tang AH, Milner TA, Alger BE. Synaptic cross talk between
713 perisomatic-targeting interneuron classes expressing cholecystokinin and
714 parvalbumin in hippocampus. Journal of Neuroscience. 2009;29:4140–54.

715 21. Guan A, Wang S, Huang A, Qiu C, Li Y, Li X, et al. The role of gamma oscillations
716 in central nervous system diseases: Mechanism and treatment. Front Cell Neurosci.
717 2022;16:962967.

718 22. Cserép C, Pósfai B, Lénárt N, Fekete R, László ZI, Lele Z, et al. Microglia monitor
719 and protect neuronal function through specialized somatic purinergic junctions.
720 Science (1979) [Internet]. 2020;367:528–37. Available from: https://www.science.org

721 23. Cserép C, Pósfai B, Dénes Á. Shaping Neuronal Fate: Functional Heterogeneity
722 of Direct Microglia-Neuron Interactions. Neuron. Cell Press; 2021. p. 222–40.

723 24. De Haan W, Van der Flier WM, Koene T, Smits LL, Scheltens P, Stam CJ. Disrupted
724 modular brain dynamics reflect cognitive dysfunction in Alzheimer's disease.
725 Neuroimage. 2012;59:3085–93.

726 25. Smailovic U, Koenig T, Kåreholt I, Andersson T, Gregoric M, Winblad B, et al.
727 Neurobiology of Aging Quantitative EEG power and synchronization correlate with
728 Alzheimer ' s disease CSF biomarkers. Neurobiol Aging. 2018;63:88–95.

729 26. Colgin LL, Moser EI. Gamma oscillations in the hippocampus. Physiology.
730 2010;25:319–29.

731 27. Jensen O, Kaiser J, Lachaux JP. Human gamma-frequency oscillations associated
732 with attention and memory. Trends Neurosci. 2007;30:317–24.

733 28. Düzel E, Penny WD, Burgess N. Brain oscillations and memory. Curr Opin
734 Neurobiol. 2010;20:143–9.

735 29. Arroyo-García LE, Isla AG, Andrade-Talavera Y, Balleza-Tapia Hugo, Raúl Loera-
736 Valencia, Laura Alvarez-Jimenez, et al. Impaired spike-gamma coupling of area CA3
737 fast-spiking interneurons as the earliest functional impairment in the App NL-G-F
738 mouse model of Alzheimer ' s disease. Mol Psychiatry [Internet]. 2021;1–11. Available
739 from: http://dx.doi.org/10.1038/s41380-021-01257-0

740 30. Arroyo-García LE, Bachiller S, Ruiz R, Boza-Serrano A, Rodríguez-Moreno A,
741 Deierborg T, et al. Targeting galectin-3 to counteract spike-phase uncoupling of fast-
742 spiking interneurons to gamma oscillations in Alzheimer's disease. Transl
743 Neurodegener. 2023;12:6.

31. Emre C, Arroyo-García LE, Do K V., Jun B, Ohshima M, Alcalde SG, et al. Intranasal delivery of pro-resolving lipid mediators rescues memory and gamma oscillation impairment in App NL-G-F/NL-G-F mice. Commun Biol. 2022;5.

32. Saito T, Matsuba Y, Mihira N, Takano J, Nilsson P, Itohara S, et al. Single App knock-in mouse models of Alzheimer's disease. Nat Neurosci. 2014;17:661–3.

33. Arroyo-García LE, Bachiller S, Ruiz R, Boza-Serrano A, Rodríguez-Moreno A, Deierborg T, et al. Targeting galectin-3 to counteract spike-phase uncoupling of fast-spiking interneurons to gamma oscillations in Alzheimer's disease. Transl Neurodegener. 2023;12.

34. Balleza-Tapia H, Arroyo-García LE, Isla AG, Loera-Valencia R, Fisahn A. Functionally-distinct pyramidal cell subpopulations during gamma oscillations in mouse hippocampal area CA3. Prog Neurobiol. 2022;210.

35. Wu T, Hu E, Xu S, Chen M, Guo P, Dai Z, et al. clusterPro fi ler 4 . 0 : A universal enrichment tool for interpreting omics data clusterPro fi ler 4 . 0 : A universal enrichment tool for interpreting omics data. The Innovation. 2021;2:100141.

36. Among T, Clusters G, Yu G. clusterProfiler : an R Package for Comparing Biological. 2012;16:284–7.

37. Minatohara K, Akiyoshi M, Okuno H. Role of immediate-early genes in synaptic plasticity and neuronal ensembles underlying the memory trace. Front Mol Neurosci. 2016;8.

38. Yap EL, Greenberg ME. Activity-Regulated Transcription: Bridging the Gap between Neural Activity and Behavior. Neuron. Cell Press; 2018. p. 330–48.

39. Kim S, Kim H, Um JW. Synapse development organized by neuronal activity-regulated immediate-early genes. Exp Mol Med. Nature Publishing Group; 2018.

40. Gallo FT, Katche C, Morici JF, Medina JH, Weisstaub N V. Immediate early genes, memory and psychiatric disorders: Focus on c-Fos, Egr1 and Arc. Front Behav Neurosci. 2018;12.

41. Dickey CA, Gordon MN, Mason JE, Wilson NJ, Diamond DM, Guzowskià JF, et al. Amyloid suppresses induction of genes critical for memory consolidation in APP + PS1 transgenic mice. J Neurochem [Internet]. 2004;88:434–42. Available from: https://onlinelibrary.wiley.com/terms-and-conditions

42. Cardin JA, Carlén M, Meletis K, Knoblich U, Zhang F, Deisseroth K, et al. Driving fast-spiking cells induces gamma rhythm and controls sensory responses. Nature. 2009;459:663–7.

43. Li Y, Zhu K, Li N, Wang X, Xiao X, Li L, et al. Reversible GABAergic dysfunction involved in hippocampal hyperactivity predicts early-stage Alzheimer disease in a mouse model. Alzheimers Res Ther. 2021;13.

44. Hu H, Gan J, Jonas P. Fast-spiking, parvalbumin + GABAergic interneurons: From cellular design to microcircuit function. Science (1979) [Internet]. 2014;345:1255263. Available from: https://www.science.org

45. Labro AJ, Priest MF, Lacroix JJ, Snyders DJ, Bezanilla F. Kv 3.1 uses a timely resurgent K + current to secure action potential repolarization. Nat Commun. 2015;6.

46. Kaczmarek LK, Zhang Y. Kv3 channels: Enablers of rapid firing, neurotransmitter release, and neuronal endurance. Physiol Rev. 2017;97:1431–68.

788 47. Andrade-Talavera Y, Arroyo-García LE, Chen G, Johansson J, Fisahn A.
789 Modulation of Kv3.1/Kv3.2 promotes gamma oscillations by rescuing Aβ-induced
790 desynchronization of fast-spiking interneuron firing in an AD mouse model in vitro.
791 Journal of Physiology. 2020;598:3711–25.

792 48. Georgiev D, González-Burgos G, Kikuchi M, Minabe Y, Lewis DA, Hashimoto T.
793 Selective expression of KCNS3 potassium channel α-subunit in parvalbumin-
794 containing GABA neurons in the human prefrontal cortex. PLoS One. 2012;7.

795 49. Miyamae T, Hashimoto T, Abraham M, Kawabata R, Koshikizawa S, Bian Y, et al.
796 Kcns3 deficiency disrupts Parvalbumin neuron physiology in mouse prefrontal cortex:
797 Implications for the pathophysiology of schizophrenia. Neurobiol Dis. 2021;155.

798 50. Martin MS, Dutt K, Papale LA, Dubé CM, Dutton SB, De Haan G, et al. Altered
799 function of the SCN1A voltage-gated sodium channel leads to γ-aminobutyric acid-
800 ergic (GABAergic) interneuron abnormalities. Journal of Biological Chemistry.
801 2010;285:9823–34.

802 51. Holmes GL, Bender AC, Wu EX, Scott RC, Lenck-Santini PP, Morse RP.
803 Maturation of EEG oscillations in children with sodium channel mutations. Brain Dev.
804 2012;34:469–77.

805 52. Vullhorst D, Neddens J, Karavanova I, Tricoire L, Petralia RS, McBain CJ, et al.
806 Selective expression of ErbB4 in interneurons, but not pyramidal cells, of the rodent
807 hippocampus. Journal of Neuroscience. 2009;29:12255–64.

808 53. Robinson HL, Tan Z, Santiago-Marrero I, Arzola EP, Dong TV, Xiong WC, et al.
809 Neuregulin 1 and ErbB4 Kinase Actively Regulate Sharp Wave Ripples in the
810 Hippocampus. Journal of Neuroscience. 2022;42:390–404.

811 54. Tan Z, Robinson HL, Yin DM, Liu Y, Liu F, Wang H, et al. Dynamic ErbB4 Activity
812 in Hippocampal-Prefrontal Synchrony and Top-Down Attention in Rodents. Neuron.
813 2018;98:380-393.e4.

814 55. Zhang H, Zhang L, Zhou D, He X, Wang D, Pan H, et al. Ablating ErbB4 in PV
815 neurons attenuates synaptic and cognitive deficits in an animal model of Alzheimer's
816 disease. Neurobiol Dis. 2017;106:171–80.

817 56. Olsen RW, Sieghart W. GABAA receptors: Subtypes provide diversity of function
818 and pharmacology. Neuropharmacology. 2009. p. 141–8.

819 57. Kujala J, Jung J, Bouvard S, Lecaignard F, Lothe A, Bouet R, et al. Gamma
820 oscillations in V1 are correlated with GABAA receptor density: A multi-modal MEG and
821 Flumazenil-PET study. Sci Rep. 2015;5.

822 58. Chen C, Arai I, Satterfield R, Young SM, Jonas P. Synaptotagmin 2 Is the Fast
823 Ca2+ Sensor at a Central Inhibitory Synapse. Cell Rep. 2017;18:723–36.

824 59. Pang ZP, Melicoff E, Padgett D, Liu Y, Teich AF, Dickey BF, et al. Synaptotagmin-
825 2 is essential for survival and contributes to Ca 2+ triggering of neurotransmitter
826 release in central and neuromuscular synapses. Journal of Neuroscience.
827 2006;26:13493–504.

828 60. Sommeijer JP, Levelt CN. Synaptotagmin-2 is a reliable marker for parvalbumin
829 positive inhibitory boutons in the mouse visual cortex. PLoS One. 2012;7.

830 61. Maximov A. Synaptotagmins. In: Squire R., editor. Encyclopedia of Neuroscience,.
831 Academic Pres; 2009. p. 819–21.

832 62. Verret L, Mann EO, Hang GB, Barth AMI, Cobos I, Ho K, et al. Inhibitory
833 Interneuron Deficit Links Altered Network Activity and Cognitive Dysfunction in
834 Alzheimer Model. Cell. 2012;149:708–21.

835 63. Sarlus H, Heneka MT, Sarlus H, Heneka MT. Microglia in Alzheimer ' s disease
836 Microglia in Alzheimer ' s disease. J Clin Invest. 2017;127:3240–9.

837 64. Frigerio CS, Wolfs L, Fattorelli N, Perry VH, Fiers M, Strooper B De, et al. The
838 Major Risk Factors for Alzheimer ' s Disease : Age , Sex , and Genes Modulate the
839 Microglia Response to A b Plaques Resource The Major Risk Factors for Alzheimer '
840 s Disease : Age , Sex , and Genes Modulate the Microglia Response to A b Plaques.
841 2019;1293–306.

842 65. Hammond TR, Dufort C, Dissing-Olesen L, Giera S, Young A, Wysoker A, et al.
843 Single-Cell RNA Sequencing of Microglia throughout the Mouse Lifespan and in the
844 Injured Brain Reveals Complex Cell-State Changes. Immunity. 2019;50:253-271.e6.

845 66. Sun N, Victor MB, Park YP, Xiong X, Scannail AN, Leary N, et al. Human microglial
846 state dynamics in Alzheimer's disease progression. Cell. 2023;186:4386-4403.e29.

847 67. Jurga AM, Paleczna M, Kuter KZ. Overview of General and Discriminating Markers
848 of Differential Microglia Phenotypes. Front Cell Neurosci. 2020;14:1–18.

849 68. Szalay G, Martinecz B, Lénárt N, Környei Z, Orsolits B, Judák L, et al. Microglia
850 protect against brain injury and their selective elimination dysregulates neuronal
851 network activity after stroke. Nat Commun. 2016;7.

852 69. Huang Y, Happonen KE, Burrola PG, O'Connor C, Hah N, Huang L, et al. Microglia
853 use TAM receptors to detect and engulf amyloid β plaques. Nat Immunol.
854 2021;22:586–94.

855 70. Casali BT, MacPherson KP, Reed-Geaghan EG, Landreth GE. Microglia depletion
856 rapidly and reversibly alters amyloid pathology by modification of plaque compaction
857 and morphologies. Neurobiol Dis. 2020;142:104956.

858 71. Spangenberg E, Severson PL, Hohsfield LA, Crapser J, Zhang J, Burton EA, et al.
859 Sustained microglial depletion with CSF1R inhibitor impairs parenchymal plaque
860 development in an Alzheimer's disease model. Nat Commun. 2019;10:3758.

861 72. Baik SH, Kang S, Son SM, Mook-Jung I. Microglia contributes to plaque growth by
862 cell death due to uptake of amyloid β in the brain of Alzheimer's disease mouse model.
863 Glia. 2016;64:2274–90.

864 73. Onuska KM. The Dual Role of Microglia in the Progression of Alzheimer ' s
865 Disease. J Neurosci. 2020;40:1608–10.

866 74. Mander PK, Jekabsone A, Brown GC. Microglia Proliferation Is Regulated by
867 Hydrogen Peroxide from NADPH Oxidase. The Journal of Immunology.
868 2006;176:1046–52.

869 75. Sun J, Zheng JH, Zhao M, Lee S, Goldstein H. Increased In Vivo Activation of
870 Microglia and Astrocytes in the Brains of Mice Transgenic for an Infectious R5 Human
871 Immunodeficiency Virus Type 1 Provirus and for CD4-Specific Expression of Human
872 Cyclin T1 in Response to Stimulation by Lipopolysaccharides. J Virol. 2008;82:5562–
873 72.

874 76. Ferretti MT, Bruno MA, Ducatenzeiler A, Klein WL, Cuello AC. Intracellular Aβ-
875 oligomers and early inflammation in a model of Alzheimer's disease. Neurobiol Aging.
876 2012;33:1329–42.

877 77. Wright AL, Zinn R, Hohensinn B, Konen LM, Beynon SB, Tan RP, et al.
878 Neuroinflammation and Neuronal Loss Precede Aβ Plaque Deposition in the hAPP-
879 J20 Mouse Model of Alzheimer's Disease. PLoS One. 2013;8.

880 78. Spangenberg EE, Green KN. Inflammation in Alzheimer's disease: Lessons
881 learned from microglia-depletion models. Brain Behav Immun. 2017;61:1–11.

882 79. Badimon A, Strasburger HJ, Ayata P, Chen X, Nair A, Ikegami A, et al. Negative
883 feedback control of neuronal activity by microglia. Nature [Internet]. 2020;586:417–23.
884 Available from: http://dx.doi.org/10.1038/s41586-020-2777-8

885 80. Pósfai B, Cserép C, Orsolits B, Dénes Á. New Insights into Microglia – Neuron
886 Interactions : A Neuron ' s Perspective. Neuroscience. 2019;405:103–17.

887 81. McBain CJ. Interneurons unbound. Nat Rev Neurosci. 2001;2:11–23.

888 82. Pelkey KA, Chittajallu R, Craig MT, Tricoire L, Wester JC, McBain CJ. Hippocampal
889 gabaergic inhibitory interneurons. Physiol Rev. 2017;97:1619–747.

890 83. Freund TF, Buzsáki G. Interneurons of the Hippocampus. Hippocampus.
891 1996;6:347–470.

892 84. Tremblay R, Lee S, Rudy B. Review GABAergic Interneurons in the Neocortex :
893 From Cellular Properties to Circuits. Neuron. 2016;91:260–92.

894 85. Mably AJ, Colgin LL. Gamma oscillations in cognitive disorders. Curr Opin
895 Neurobiol. 2018;52:182–7.

896 86. Kurudenkandy FR, Zilberter M, Biverstål H, Presto J, Honcharenko D, Strömberg
897 R, et al. Amyloid-β-induced action potential desynchronization and degradation of
898 hippocampal gamma oscillations is prevented by interference with peptide
899 conformation change and aggregation. Journal of Neuroscience. 2014;34:11416–25.

900 87. Klemz A, Wildner F, Tütüncü E, Gerevich Z. Regulation of Hippocampal Gamma
901 Oscillations by Modulation of Intrinsic Neuronal Excitability. Front Neural Circuits.
902 2022;15.

903 88. Traynelis SF, Wollmuth LP, McBain CJ, Menniti FS, Vance KM, Ogden KK, et al.
904 Glutamate receptor ion channels: Structure, regulation, and function. Pharmacol Rev.
905 2010. p. 405–96.

906 89. Rao VR, Pintchovski SA, Chin J, Peebles CL, Mitra S, Finkbeiner S. AMPA
907 receptors regulate transcription of the plasticity-related immediate-early gene Arc. Nat
908 Neurosci. 2006;9:887–95.

909

910

911

912 **Figure and table legends**

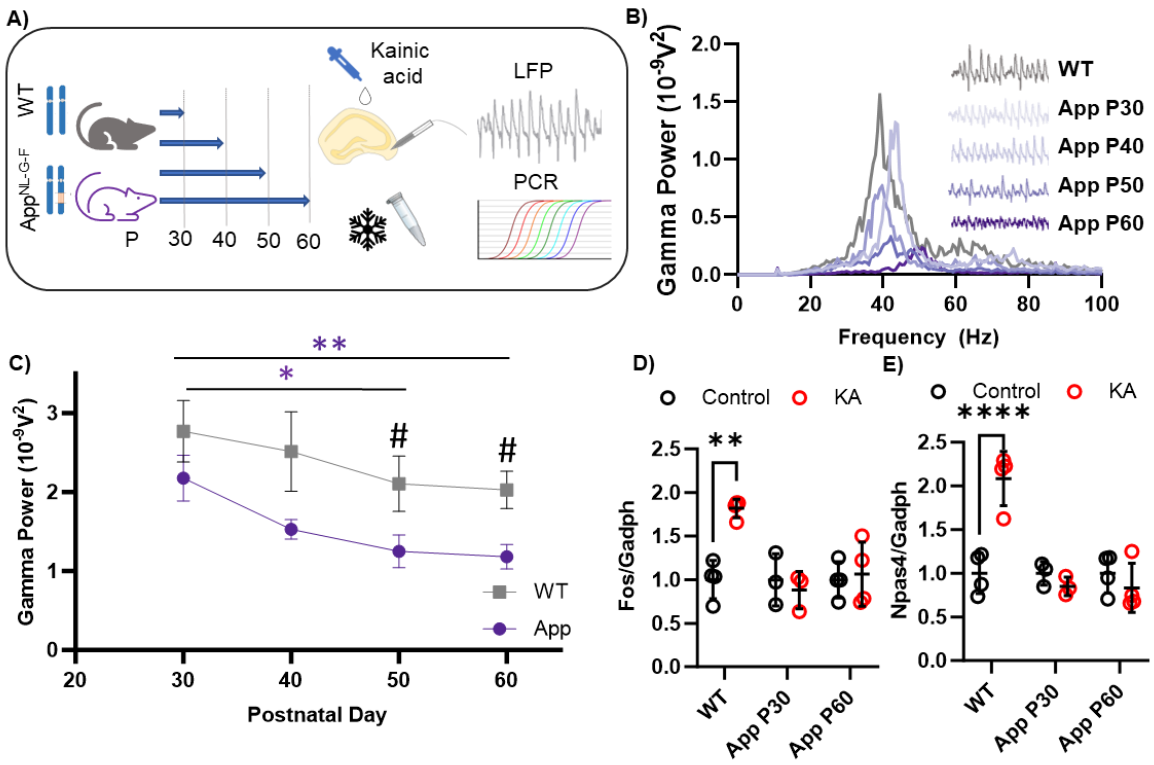

913

914 **Fig 1 - Progressive impairment of Hippocampal gamma oscillations in *App*$^{NL\text{-}G\text{-}F}$**

915 **mice.**

916 **A)** Graphic methods for LFP recordings and PCR. **B)** Representative power spectra

917 from WT and *App*$^{NL\text{-}G\text{-}F}$ at different ages. **C)** Line plot of gamma oscillation power in

918 WT and *App*$^{NL\text{-}G\text{-}F}$ mice at different ages showing a progressive decrease of the

919 hippocampal network synchrony in *App*$^{NL\text{-}G\text{-}F}$ mice. The graph shows a two-way

920 ANOVA with Holm–Sidak's multiple comparisons test at P30 (WT n= 6 vs *App*$^{NL\text{-}G\text{-}F}$

921 n=6, p=0,124), P40 (WT n= 6 vs *App*$^{NL\text{-}G\text{-}F}$ n=6, p=0,172), P50 (WT n= 6 vs *App*$^{NL\text{-}G\text{-}F}$

922 n=9, p=0,017), and P60 (WT n= 7 vs *App*$^{NL\text{-}G\text{-}F}$ n=11, p=0,010) (# signficance). Intra-

923 group differences were evaluated too: for the WT group P30 vs P40 (p= 0,287), P30

924 vs P50 (p= 0,304), P30 vs P60 (p=0,255). For the *App*$^{NL\text{-}G\text{-}F}$ group P30 vs P40 (p=

925 0,326), P30 vs P50 (p= 0,049), P30 vs P60 (p= 0,026) (* significance). **D)** Two-way

926 ANOVA with Holm–Sidak's multiple comparisons test for *Fos* normalized expression
927 showing overexpression in WT KA-exposed slices (WT control n=4 vs KA n=4, p=
928 0,003) but not in *App*$^{NL\text{-}G\text{-}F}$ KA - exposed slices (*App*$^{NL\text{-}G\text{-}F}$ P30 control n=3 vs KA n=3,
929 p=0,999; *App*$^{NL\text{-}G\text{-}F}$ F P60 n=4 control vs KA n=4, p=0,999). **E)** Two-way ANOVA with
930 Holm–Sidak's multiple comparisons test for *Npas4* normalized expression showing
931 overexpression in WT KA-exposed slices (WT control n=4 vs KA n=4, p<0,0001) but
932 not in *App*$^{NL\text{-}G\text{-}F}$ KA - exposed slices (*App*$^{NL\text{-}G\text{-}F}$ P30 control n=3 vs KA n=3, p=0,983;
933 *App*$^{NL\text{-}G\text{-}F}$ P60 n=3 control vs KA n=3, p=0,983). Data are presented as mean ± SEM,
934 and "n" indicates the number of mice. *p < 0,05, #p < 0,05, **p < 0,01, ***p < 0,001,
935 **** p < 0,0001.

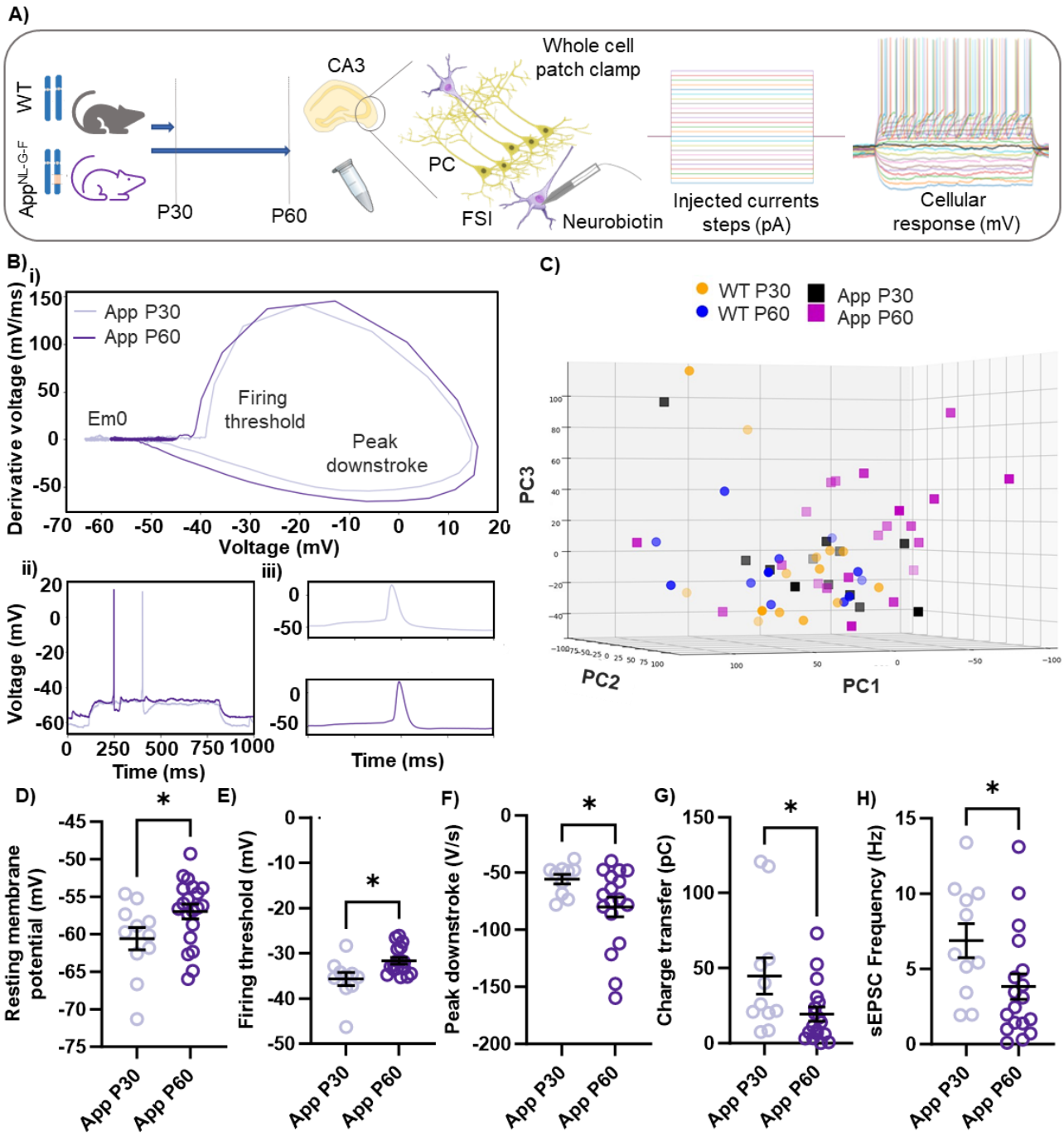

Fig 2 - Fast-spiking interneurons intrinsic properties and postsynaptic input change during amyloid pathology progression.

A) Graphic methods for whole cell patch clamp recordings from FSI. **B.i)** Representative phase-plot of the FSI's action potentials from *App*$^{NL\text{-}G\text{-}F}$ mice at P30

941 and P60 showing different action potential shape and resting membrane potential
942 (Em0) in the two groups. **B.ii)** Current-clamp recording traces of the representative
943 FSI in B.i. **B.iii)** Cropped recording of the action potential of the FSI in Bi-ii. **C)** PCA of
944 the intrinsic properties of WT P30 (n= 17), WT P60 (n= 11), *App*$^{NL\text{-}G\text{-}F}$ P30 (n=10), and
945 *App*$^{NL\text{-}G\text{-}F}$ P60 (n=17) FSI. PC1 accounts for 37% of variation, PC2 for 34% and PC3
946 for 19%. *App*$^{NL\text{-}G\text{-}F}$ P60 FSI exhibit distinct properties that make them cluster separately
947 from the other groups. **D-H)** Scatter plots of unpaired t-test of FSI's intrinsic properties
948 and post-synaptic input in the *App*$^{NL\text{-}G\text{-}F}$ group (P30 n=11 vs P60 n=17), showing **D)**
949 resting membrane potential (p=0,044), **E)** firing threshold (p=0,011), **F)** peak
950 downstroke (p=0,048), **G)** charge transfer (p=0,030), **H)** sEPSC frequency (p=0,049).
951 Data are presented as mean ± SEM, and "n" indicates the number of neurons. *p <
952 0,05, **p < 0,01, ***p < 0,001.

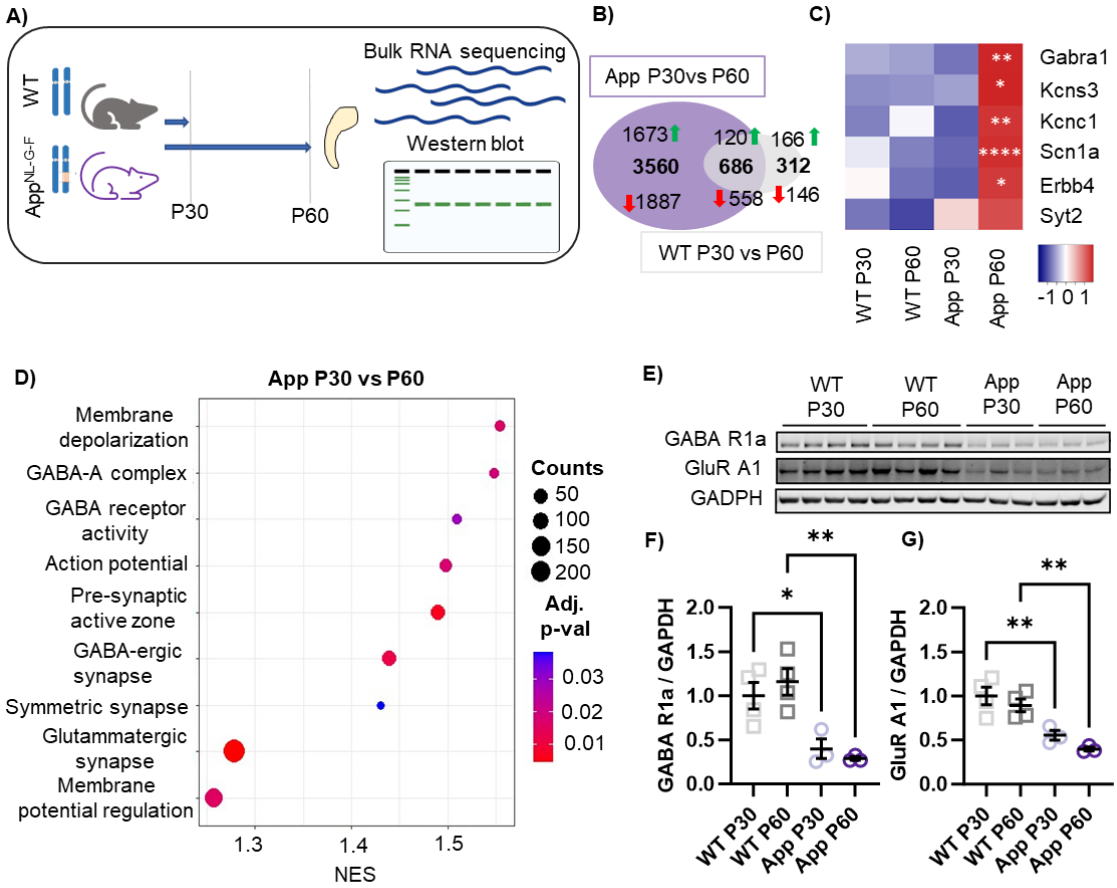

953

954 **Fig 3 - Bulk RNA sequencing reveals synaptic-related transcriptional changes**
955 **during the early stage of amyloid pathology progression.**

956 **A)** Graphic methods for bulk RNA sequencing and western blot analysis from whole
957 hippocampal tissue. **B)** Venn diagram showing unique and overlapping transcriptional
958 changes between WT P30 vs P60 and *App*$^{NL\text{-}G\text{-}F}$ P30vs P60. The green arrows indicate
959 upregulated genes and the red arrows indicate downregulated genes. **C)** Heat map
960 showing the differences in the normalized count of selected genes relevant for FSI's
961 functionality and gamma oscillation onset in WT P30 (n=4), WT P60 (n=4), *App*$^{NL\text{-}G\text{-}F}$
962 P30 (n=4), *App*$^{NL\text{-}G\text{-}F}$ P60 (n=4). The significance level indicates the comparison of
963 *App*$^{NL\text{-}G\text{-}F}$ P30 vs P60 of *Gabra1* (Log2FC=0,252, p= 0,002), *Kcns3* (Log2FC=0,216,
964 p= 0,031), *Kcnc1* (Log2FC=0,282, p= 0,0002), *Scn1a* (Log2FC=0,393, p<0,0001),
965 *Erbb4* (Log2FC=0,269, p= 0,016), *Syt2* (Log2FC=0,209, p= 0,118) obtained from the
966 Wald test. **D)** Dot plot of the gene set enrichment analysis in *App*$^{NL\text{-}G\text{-}F}$ P30 vs P60,
967 showing changes involving synaptic transmission and neuronal excitability regulation.
968 **E)** Western blot membrane of GABA receptor 1 alpha, Glutamate receptor A1 and
969 GADPH from VT P30 (n=4), WT P60 (n=4), *App*$^{NL\text{-}G\text{-}F}$ P30 (n=4), *App*$^{NL\text{-}G\text{-}F}$ P60 (n=4).
970 **F)** Scatter plot of one-way ANOVA with Holm–Sidak's multiple comparisons test of
971 GABA R1a normalized expression showing a downregulation in *App*$^{NL\text{-}G\text{-}F}$ (WT vs
972 *App*$^{NL\text{-}G\text{-}F}$ P30 p= 0,034; WT vs *App*$^{NL\text{-}G\text{-}F}$ P60 p= 0,005; *App*$^{NL\text{-}G\text{-}F}$ P30 vs P60,
973 p=0,9466) **G)**. Scatter plot of one-way ANOVA with Holm–Sidak's multiple
974 comparisons test of GluR A1 protein level showing a decrease in *App*$^{NL\text{-}G\text{-}F}$ (WT vs
975 *App*$^{NL\text{-}G\text{-}F}$ P30 p= 0,009; WT vs *App*$^{NL\text{-}G\text{-}F}$ P60 p=0,005; *App*$^{NL\text{-}G\text{-}F}$ P30 vs P60,
976 p=0,561). Scatter plots data are presented as mean ± SEM, and "n" indicates the
977 number of animals. *p < 0,05, **p < 0,01, ***p < 0,001, **** p < 0,0001.

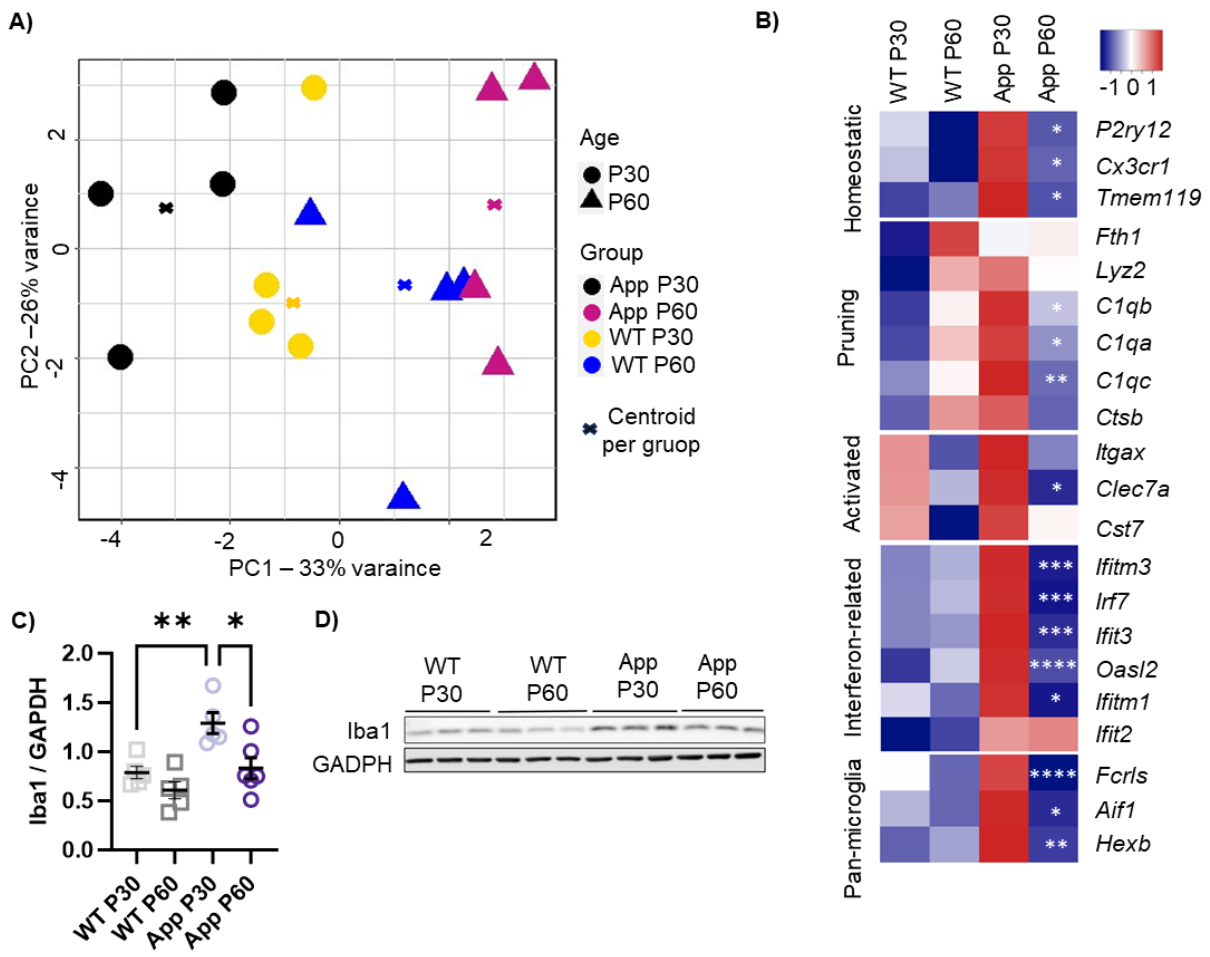

Fig 4 - Microglia-related transcriptional changes indicate loss of homeostatic and inflammatory microglia during the early stage of amyloid pathology progression.

A) PCA of 2054 microglia-related gene expression in WT P30 (n= 4), WT P60 (n= 4), *App*$^{NL\text{-}G\text{-}F}$ P30 (n=4), *App*$^{NL\text{-}G\text{-}F}$ P60 (n=4). Centroids represent the geometrical centre of each group. **B)** Heat maps showing the differences in the normalized count of microglial genes associated with different microglia phenotypes in WT P30 (n=4), WT P60 (n=4), *App*$^{NL\text{-}G\text{-}F}$ P30 (n=4), *App*$^{NL\text{-}G\text{-}F}$ P60 (n=4). The significance level indicates the comparison of *App*$^{NL\text{-}G\text{-}F}$ P30 vs P60 of *P2ry12* (Log2FC= -0,205, p= 0,031), *Cx3cr1* (Log2FC= -0,206, p= 0,026) and *Tmem119* (Log2FC= -0,213, p= 0,023), for

989 homeostatic microglia; *Fth1* (Log2FC= -0,020, p= 0,872), *Lyz2* (Log2FC= -0,054, p=
990 0,657), *C1qb* (Log2FC= -0,196, p= 0,004), *C1qa* (Log2FC= -0,216, p= 0,031), *C1qc*
991 (Log2FC= -0,270, p= 0,002), *Ctsb* (Log2FC= -0,082, p= 0,100) for homeostatic
992 microglia engaged in synaptic pruning; *Itgax* (Log2FC= -0,097, p= 0,150), *Clec7a*
993 (Log2FC= -0,329, p= 0,035), *Cst* (Log2FC= 0,158, p= 0,33) for activated microglia;
994 *Iftitm3* (Log2FC= -0,593, p= 0,0001), *Irf7* (Log2FC= -0,745, p= 0,0005), *Ifit3* (Log2FC=
995 -0,560, p= 0,0009), *Oasl2* (Log2FC= -0,649, p<0,00001), *Ifitm1* (Log2FC= -0,681, p=
996 0,011), *Ifit2* (Log2FC= 0,078, p= 0,956) for interferon related microglia; *Fcrls* (Log2FC=
997 -0,448, p<0,00001), *Aif1* (Log2FC= -0,257, p= 0,018), *Hexb* (Log2FC= -0,234, p=
998 0,009) for pan-microglia. **C)** Scatter plot of one-way ANOVA with Holm–Sidak's
999 multiple comparisons test of Iba1 normalized protein level showing an increase in
1000 $App^{NL\text{-}G\text{-}F}$ at P30 (WT n=5 vs $App^{NL\text{-}G\text{-}F}$ n=5, p= 0,009) and a decrease in $App^{NL\text{-}G\text{-}F}$ at
1001 P60 ($App^{NL\text{-}G\text{-}F}$ P30 n=5 vs P60 n=6, p= 0,011). **D)** Representative western blot
1002 membrane of Iba1 and GADPH from WT P30 (n=3), P60 (n=3), and $App^{NL\text{-}G\text{-}F}$ P30
1003 (n=3), P60 (n=3). Scatter plot data are presented as mean ± SEM, and "n" indicates
1004 the number of animals. *p < 0,05, **p < 0,01, ***p < 0,001, **** p < 0,0001.

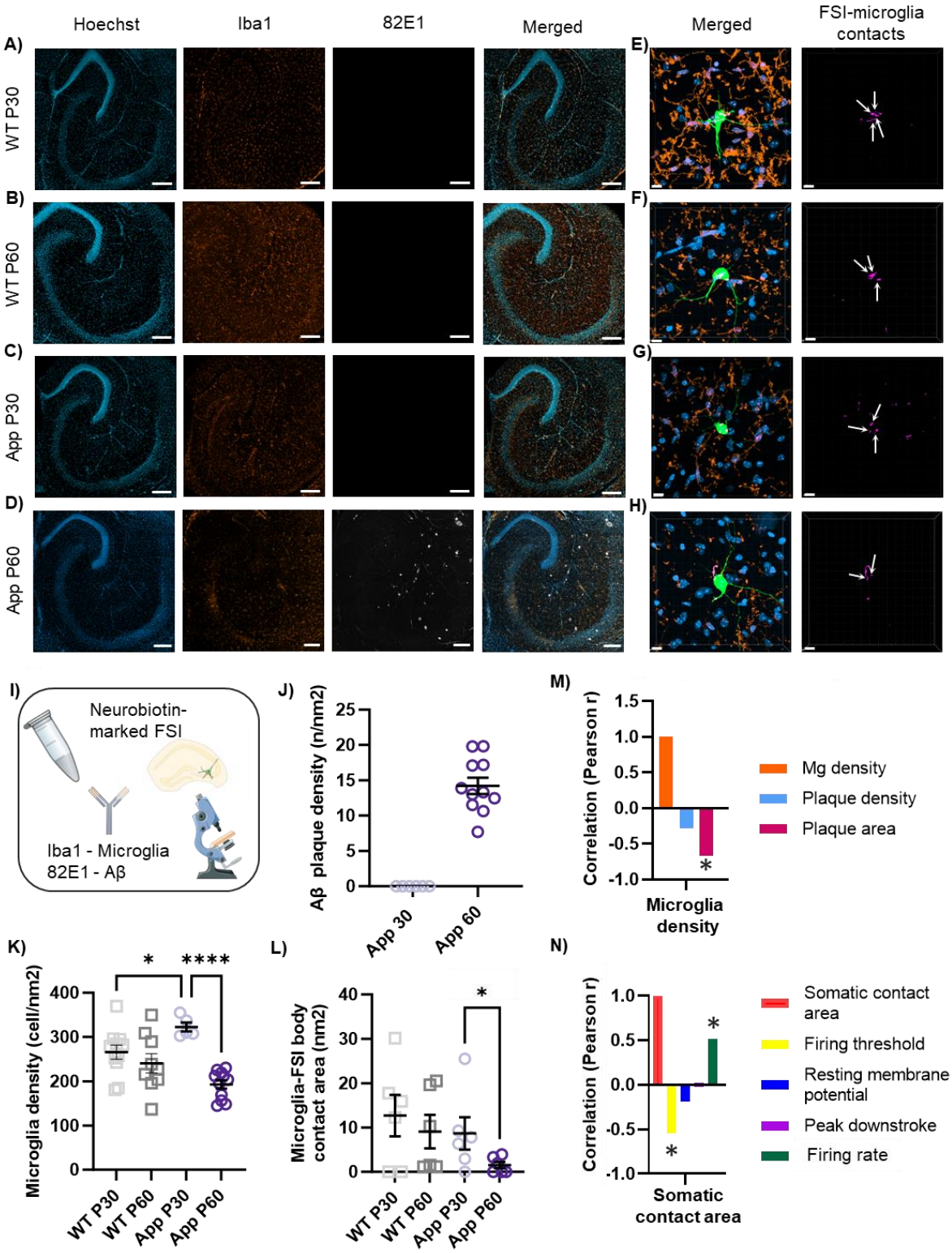
Hoechst
Iba1
82E1
Merged
Merged
FSI-microglia contacts
A)
B)
C)
D)
E)
F)
G)
H)
WT P30
WT P60
App P30
App P60
I)
Neurobiotin-marked FSI
Iba1 - Microglia
82E1 - Aβ
J)
Aβ plaque density (n/nm2)
App 30
App 60
M)
Correlation (Pearson r)
Microglia density
Mg density
Plaque density
Plaque area
K)
Microglia density (cell/nm2)
WT P30
WT P60
App P30
App P60
L)
Microglia-FSI body contact area (nm2)
N)
Correlation (Pearson r)
Somatic contact area
Somatic contact area
Firing threshold
Resting membrane potential
Peak downstroke
Firing rate

1005

1006

1007 **Fig 5 - Iba1-positive microglia density decreases during the early stage of**
1008 **amyloid pathology and correlates with plaque aggregation and FSI dysfunction.**

1009 **A-D)** Representative immunofluorescent staining of nuclei (Hoechst - blue), microglia
1010 (Iba1-red), Aβ (82E1-white) in the hippocampus of **A)** WT P30 (n= 11), **B)** WT P60
1011 (n=9), **C)** *App*$^{NL\text{-}G\text{-}F}$ P30 (n=6) and **D)** *App*$^{NL\text{-}G\text{-}F}$ P30 (n=11). **E-H)** Imaris 3D
1012 reconstruction of neurobiotin-marked FSI (green), microglia (Iba1-red), nuclei
1013 (Hoechs-blue) and FSI-microglia contacts (pink) in **E)** WT P30 (n= 6), **F)** WT P60
1014 (n=6), **G)** *App*$^{NL\text{-}G\text{-}F}$ P30 (n=6) and **H)** *App*$^{NL\text{-}G\text{-}F}$ P30 (n=6). **I)** Graphic method for
1015 immunofluorescent staining. **J)** Scatter-plot showing Aβ plaque density in the
1016 hippocampus of *App*$^{NL\text{-}G\text{-}F}$ P30 and *App*$^{NL\text{-}G\text{-}F}$ P60. **K)** Scatter-plot of one-way ANOVA
1017 with Holm–Sidak's multiple comparisons test of microglia density, which increases in
1018 *App*$^{NL\text{-}G\text{-}F}$ P30 (WT P30 vs *App*$^{NL\text{-}G\text{-}F}$ P30 p= 0,036) and decreases in *App*$^{NL\text{-}G\text{-}F}$ P60
1019 (WT P60 vs *App*$^{NL\text{-}G\text{-}F}$ P30 p= 0,065, *App*$^{NL\text{-}G\text{-}F}$ P30 vs *App*$^{NL\text{-}G\text{-}F}$ P60 p<0,0001). **L)**
1020 Scatter-plot of one-tail unpaired t-test of FSI-microglia somatic contact area in WT and
1021 *App*$^{NL\text{-}G\text{-}F}$ groups showing a decrease in *App*$^{NL\text{-}G\text{-}F}$ P60 (*App*$^{NL\text{-}G\text{-}F}$ P30 vs P60,
1022 p=0,0418). **M)** Bar-plot of Pearson correlation test of microglia density with Aβ plaque
1023 density and Aβ plaque area in the hippocampus of *App*$^{NL\text{-}G\text{-}F}$ P60. Microglia density
1024 inversely correlates with Aβ plaque area (correlation score r =-0,671; p=0,048). **N)** Bar-
1025 plot of Pearson correlation test of microglia-FSI somatic contact area and FSI firing
1026 threshold, resting membrane potential, peak downstroke, and firing frequency of FSI
1027 regardless of the group (n=19). Microglia-FSI somatic contact area inversely
1028 correlates with FSI firing threshold (correlation score r=-0,548; p=0,015) and directly
1029 correlates with FSI's firing frequency (correlation score r=0,519; p=0,023). Scatter-plot
1030 data are presented as mean ± SEM, "n" indicates the number of slices in A-D, L, N

and the number of neurons in E-G, M, O. Scale-bar represents 200µm in A-D and 10µm in E-H. *p < 0,05, **p < 0,01, ***p < 0,001, **** p < 0,0001.

Table 1

	Rheobase (pA)	Firing latency (ms)	Firing threshold (mV)	AP amplitude (mV)	AP Half-width (ms)	Peak upstroke (V/s)	Peak downstroke (V/s)
WT P30 (n=17)	43,13 ± 4,892	93,96 ± 12,98	-35,92 ± 1,725	58,25 ± 2,495	1,14 ± 0,066	148,7 ± 9,367	-63,60 ± 4,827
WT P60 (n=11)	53,64 ± 7,600	53,64 ± 7,660	-35,84 ± 1,485	56,50 ± 1,498	1,25 ± 0,087	140,1 ± 7,019	-58,32 ± 6,397
App P30 (n=11)	35,45 ± 5,934	179,5 ± 25,490	-35,67 ± 1,437	48,48 ± 3,337	1,16 ± 0,095	128,1 ± 9,510	-54,12 ± 4,141
App P60 (n=17)	49,1 ± 6,832	155,9 ± 32,040	-31,67 ± 0,733	47,41 ± 2,631	0,97 ± 0,079	130,9 ± 7,506	-80,08 ± 8,594

	Rise rate	Fall rate	Rise time (ms)	Firing rate (Hz)	Em 0 (mV)	Input resistance (GΩ)	Sag (mv)
WT P30 (n=17)	97,48 ± 6,367	-38,35 ± 3,260	0,6211 ± 0,025	6,846 ± 0,768	-57,57 ± 1,323	0,401 ± 0,060	3,685 ± 0,547
WT P60 (n=11)	87,47 ± 5,324	-31,70 ± 4,143	0,6467 ± 0,033	7,070 ± 1,109	-59,57 ± 1,516	0,342 ± 0,033	3,977 ± 0,410
App P30 (n=11)	83,54 ± 6,382	-34,02 ± 3,732	0,590 ± 0,024	10,860 ± 1,437	-60,60 ± 1,481	0,388 ± 0,035	5,457 ± 0,930
App P60 (n=17)	88,41 ± 5,302	-45,59 ± 4,555	0,594 ± 0,040	8,594 ± 1,368	-56,99 ± 0,974	0,370 ± 0,032	4,378 ± 0,570

Table 1 – Intrinsic properties of FSI

Intrinsic properties of FSI in WT P30 (n= 17), WT P60 (n=11), *App*$^{NL\text{-}G\text{-}F}$ P30 (n=11) and *App*$^{NL\text{-}G\text{-}F}$ P60 (n=17). Data are presented as mean ± SEM, and “n” indicates the number of cells.